1

Structural basis for activation of DNMT1

3

4 Hiroki Onoda[1]†, Amika Kikuchi[1]†, Kosuke Yamaguchi[2], Satomi Kori[1], Shun Matsuzawa[1], Yoshie

5 Chiba[3], Shota Tanimoto[3], Sae Yoshimi[1], Hiroki Sato[1], Atsushi Yamagata[4], Mikako Shirouzu[4],

6 Naruhiko Adachi[5], Jafar Sharif[6], Haruhiko Koseki[6], Atsuya Nishiyama[3], Makoto Nakanishi[3],

7 Pierre-Antoine Defossez[2], Kyohei Arita*[1]

8 [1]Structural Biology Laboratory, Graduate School of Medical Life Science, Yokohama City

9 University, Tsurumi-ku, Yokohama, Kanagawa, 230-0045, Japan.

10 [2] Université Paris Cité, CNRS, Epigenetics and Cell Fate, 75013 Paris, France.

11 [3] Division of Cancer Cell Biology, The Institute of Medical Science, The University of Tokyo, 4-

12 6-1 Shirokanedai, Minato-ku, Tokyo 108-8639, Japan.

13 [4] Laboratory for Protein Functional and Structural Biology, RIKEN Center for Biosystems

14 Dynamics Research, 1-7-22 Suehiro-cho, Tsurumi-ku, Yokohama, Kanagawa 230-0045, Japan.

15 [5] Structural Biology Research Center, Photon Factory, Institute of Materials Structure Science,

16 High Energy Accelerator Research Organization (KEK), Tsukuba, Ibaraki 305-0801, Japan.

17 [6] Laboratory for Developmental Genetics, RIKEN Center for Integrative Medical Sciences (IMS),

18 Yokohama, Kanagawa, Japan.

19

20 † H.O., and A.K. contributed equally.

21

22 *Corresponding author:

23 Kyohei Arita, Ph.D., Structure Biology Laboratory, Graduate School of Medical Life Science,

24 Yokohama City University, 1-7-29, Suehiro-cho, Tsurumi-ku, Yokohama, Kanagawa 230-0045,

25 Japan, E-mail: aritak@yokohama-cu.ac.jp; Tel. (+81)45-508-7225; Fax. (+81)45-508-7365.

26

1 **Abstract**

2 DNMT1 is an essential enzyme that maintains genomic DNA methylation, and its function

3 is regulated by mechanisms that are not yet fully understood. Here, we report the cryo-EM

4 structure of nearly full-length human DNMT1 bound to its two natural activators: hemimethylated

5 DNA and ubiquitinated histone H3. We find that a hitherto unstudied linker, between the RFTS

6 and CXXC domains, plays a key role for activation. It contains a conserved α-helix which engages

7 a crucial "Toggle" pocket, displacing a previously described inhibitory linker, and allowing the

8 DNA recognition helix to spring into the active conformation. This is accompanied by large-scale

9 reorganization of the inhibitory RFTS and CXXC domains, allowing the enzyme to gain full

10 activity. Our results therefore provide a mechanistic basis for the activation of DNMT1, with

11 consequences for basic research and drug design.

12

13

Introduction

DNA methylation is a key epigenetic mark that regulates gene expression and genome stability [1,2]. In mammals, DNA methylation occurs at the 5th position of cytosine, mostly within CpG dinucleotides, and it is catalyzed by a DNA methyltransferase (DNMT) family. *De novo* DNMTs (DNMT3A, 3B and 3L) set up proper DNA methylation pattern during development and differentiation, and this pattern is faithfully copied on the newly replicated DNA at each round of cell division, by the maintenance enzyme DNMT1 [3,4]. An E3 ubiquitin ligase (ubiquitin-like containing PHD and RING finger domains 1, UHRF1) protein, plays a crucial role for maintenance DNA methylation [5,6], together with DNMT1. UHRF1 recognizes hemimethylated DNA via its SET and RING-associated (SRA) [7–9] and catalyzes double monoubiquitination at K18 and K23 on histone H3 (H3Ub2) which, in turn, recruits DNMT1 and stimulates its enzymatic activity [10–14].

DNMT1 is a large protein (1616 amino acids), containing multiple domains (Fig. 1a), and subject to intramolecular regulations that strongly restrict its activity to hemimethylated DNA [15]. In the absence of DNA (apo-DNMT1), the enzyme is autoinhibited: Binding of Replication-Foci Targeting Sequence (RFTS) to the catalytic core, in association with recognition of the DNA binding region by an Auto-Inhibitory Linker, inhibit the access of hemimethylated DNA to DNMT1 catalytic region [16,17]. A key unresolved question is: how does the combined presence of H3Ub2 and hemimethylated DNA allow the enzyme to overcome this double inhibition? Of note, previous structural studies of DNMT1 in a complex with hemimethylated DNA [18–20] have used a truncated version of the protein (aa:729-1616, Fig. 1a), therefore the fate of the inhibitory regions, RFTS and Auto-Inhibitory Linker, during activation is unknown.

In order to understand the detailed molecular mechanism for DNMT1 activation, we have determined the cryogenic electron microscopy (cryo-EM) structure of nearly full-length human DNMT1 (aa:351-1616), stimulated by the H3Ub2 tail and in an intermediate complex with a hemimethylated DNA analog. Our structure illuminates the synergistic structural rearrangements that underpin the activation of DNMT1. In particular, it highlights the key role of a hydrophobic "Toggle" pocket in the catalytic domain, which stabilizes both the inactive (inhibited) or the active states. In the latter case, it functions by accepting a pair of phenylalanine residues from a hitherto unrecognized, yet highly conserved Activating Helix located between the RFTS and CXXC domains.

Results

Cryo-EM structure of DNMT1 bound to ubiquitinated H3 and hemimethylated DNA

To uncover the molecular mechanism of DNMT1 activation, we conducted cryo-EM single particle analysis of DNMT1 (aa:351-1616) in an intermediate complex with H3Ub2 tail and hemimethylated DNA (Fig. 1). The human DNMT1 protein was produced using the Sf9 baculovirus expression system, and an H3 tail peptide (aa:1-37W, K14R/K27R/K36R) was di-ubiquitinated on K18 and K23 to completion *in vitro* (Extended Data Fig. 1 and see method). As expected from previous work [12,13], the addition of H3Ub2 enhanced the enzymatic activity of DNMT1 (Extended Data Fig. 1d,e). The DNMT1:H3Ub2 binary complex was used for reaction with hemimethylated DNA. The target cytosine in hemimethylated DNA was replaced by a 5-fluorocytosine (5fC) to form an irreversible covalent complex with DNMT1 [21]. The ternary complex containing DNMT1 bound to H3Ub2 and DNA$^{mCG/fCG}$ was purified by gel-filtration chromatography (Extended Data Fig. 2), and used for cryo-EM single particle analysis (Extended Data Fig. 3).

3D variability analysis by cryoSPARC [22] revealed 2 types of particles: Type I particles with 2.5 Å resolution, in which the CXXC domain was ordered (Fig. 1b), and Type II particles with 2.2 Å resolution, in which the CXXC was disordered (Extended Data Fig. 4a). The atomic models of DNMT1 were constructed from the two types (Table 1); these structures were essentially the same (except for the CXXC domain), therefore in the rest of the paper we will focus on the Type I DNMT1 particle, with the ordered CXXC. In this structure, the RFTS domain, Auto-Inhibitory Linker, N-terminal β-sheet of BAH1 (aa:731-755) and some loops and linkers were invisible, reflecting their flexibility (Fig. 1b). The structured elements of the ternary complex showed that the catalytic core of DNMT1 bound to hemimethylated DNA, the catalytic loop (aa:1224-1238) recognized flipped-out 5fC, and the Target Recognition Domain (TRD) residues (Cys1499, Leu1500, Trp1510, Leu1513 and Met1533) bound to the methyl-group of 5mC (Extended Data Fig. 4b-d). Overall, these results confirm previously reported DNMT1:hemimethylated DNA binary complex structures (Supplementary Notes) [18–20]. In addition, they show, for the first time, the behavior of the RFTS and Auto-Inhibitory Linker in the active form, as described in the following section.

Spatial rearrangement of RFTS and CXXC domains in the active form

1   The dissociation of the RFTS domain from the catalytic core is assumed to be required

2   for DNMT1 activation, yet no direct evidence of this structural rearrangement has been shown to

3   date. Our cryo-EM structure of apo-DNMT1 (aa:351-1616) at 3.4 Å resolution showed a fully-

4   structured RFTS domain bound to the catalytic core (Extended Data Fig. 5a left, and

5   Supplementary Table 1). In contrast, the cryo-EM map of the DNMT1:H3Ub2:DNA$^{mCG/fCG}$

6   ternary complex showed no density for the RFTS:H3Ub2 (Fig. 1b). Intriguingly, particles smaller

7   than the DNMT1:H3Ub2:DNA$^{mCG/fCG}$ ternary complex were observed in 2D class average

8   (Extended Data Fig. 6a). The size and shape of these particles were comparable to those of

9   RFTS:H3Ub2 as estimated from the 2D projected template of RFTS:H3Ub2 (PDB:5WVO)-

10   derived 3D Gaussian model (Extended Data Fig. 6b). These data indicate that the RFTS:H3Ub2

11   moiety is in a highly dynamic state and does not interact with other domains when DNMT1 is

12   active.

13   To separate the contributions of H3Ub2 and of hemimethylated DNA for displacement of

14   the RFTS, we determined the cryo-EM structure of DNMT1 (aa:351-1616) in complex with

15   H3Ub2, but without DNA (Extended Data Figs. 1c, 5a right, and Supplementary Table 1). This

16   structure reached 3.6 Å resolution and showed that, while the N-lobe of DNMT1 became flexible

17   and therefore invisible, the C-lobe remained bound firmly to the catalytic core upon H3Ub2

18   binding. These data were further supported by small angle X-ray scattering (SAXS) analyses

19   (Extended Data Fig. 5b, Supplementary Fig. 6, Supplementary Table 2, and Supplementary Notes),

20   showing that H3Ub2, in itself, is not sufficient to dislodge the RFTS.

21   We next investigated the dynamics of the CXXC domain after DNMT1 activation. In apo-

22   DNMT1, the CXXC domain is affixed to the side of the RFTS domain (Fig. 2a and Extended Data

23   Fig. 7a) [16,17]. In the presence of unmethylated DNA (DNA$^{CG/CG}$) (PDB:3PTA), the zinc finger

24   motif of the CXXC domain recognizes unmethylated CpG, shifts 30 Å towards the TRD domain,

25   and sits near the active center (Fig. 2a and Extended Data Fig. 7c) [23]. In this conformation, the

26   Auto-Inhibitory Linker directly interrupts the binding of DNA to the active site, which prevents

27   unlicensed *de novo* DNA methylation. Intriguingly, in our active complex, the CXXC domain

28   moved away from the active center and took an "upside-down" position (relative to 3PTA),

29   between the BAH1 domain and the catalytic domain with which it established hydrogen bonds and

30   van der Waals interactions (Fig. 2b,c).

31   As the DNA binding interface of the CXXC remained solvent-exposed in the active

32   complex (Fig. 2a), so we asked whether it could still bind unmethylated DNA. However, the

1   superimposition of the CXXC:DNA complex onto the ternary complex structure revealed major

2   steric clashes with the catalytic domain (Fig. 2d), suggesting that DNA binding by the CXXC is

3   fully suppressed when DNMT1 is active. The new position of the CXXC leads to a structural

4   deformation of the BAH1 N-terminal β-sheet and induces a different orientation of the BAH1 loop

5   (aa:765-775) (Fig. 1b and Extended Data Fig. 7b). These structural changes then lead to full

6   eviction of the Auto-Inhibitory Linker from the catalytic core and causes the Auto-Inhibitory

7   Linker to adopt a highly disordered structure (Fig. 1b and Extended Data Fig. 7b).

8   Taken together, our cryo-EM analysis of the active form of DNMT1 revealed a large

9   reorganization of the inhibitory domains relative to unliganded or inactive forms. Upon joint

10   binding of H3Ub2 and hemimethylated DNA, the RFTS domain is forced out of the catalytic core,

11   while the CXXC domain undergoes a drastic spatial rearrangement ultimately leading to eviction

12   of the Auto-Inhibitory Linker from the catalytic core.

13

A "Toggle" pocket accepts different phenylalanines in the repressed and active states

15   Zooming in on the catalytic site, we observed another striking difference between the

16   inactive and active states of the enzyme (Fig. 3a).

17   In the inactive state, the DNA Recognition Helix (aa:1236-1259) in the catalytic domain

18   is kinked, at Ser1245 (Fig. 3b,c). A hydrophobic pocket (composed of Val1248, Phe1263, Leu1265,

19   Phe1274, Val1279, and Leu1282, hereafter Toggle Pocket) accepts Phe1235 of the catalytic loop

20   and Phe1243 of the DNA Recognition Helix. In addition, Tyr1240 within this same helix forms

21   hydrophobic interactions with Phe628, Phe631 and Phe632 from the Activating Helix (aa:620-

22   635), further stabilizing the inactive conformation (Fig. 3a).

23   This contrasts sharply with our activated form of DNMT1 (Fig. 3d,e). In that situation,

24   the Activating Helix is shortened as it forms a helix-turn; its residues Phe631 and Phe632 invade

25   the Toggle Pocket. The DNA Recognition Helix is freed from the Toggle Pocket and springs into

26   a straight conformation, which allows i) access of Phe1235/Arg1238 (in the catalytic loop) to the

27   minor groove at the mCG/fCG site, ii) formation of a hydrogen bond between Tyr1240 in the DNA

28   Recognition Helix and the phosphate backbone of the DNA and iii) engagement of Phe1243 (in

29   the DNA Recognition Helix) by Pro613, Lys617 and Gln635 (in the linker between RFTS and

30   CXXC domains), which prevents Phe1243 from entering the Toggle Pocket (Fig. 2a,b and

31   Extended Data Fig. 8a).

1   Interestingly, a previous study of human DNMT1 binary complex (aa:729-1600, not

2   containing Activating Helix) with hemimethylated DNA analog (active state, PDB: 6X9I) shows

3   that Phe1243 remains in the Toggle Pocket and the N-terminal region of the DNA Recognition

4   Helix structure is partially unfolded, thereby preventing the binding of Tyr1240 to the phosphate

5   backbone of DNA (Extended Data Fig. 8a,b) [20]. Furthermore, folded or unfolded DNA

6   Recognition Helix structures are observed in the previous structures of mouse DNMT1 (aa:731-

7   1602) bound to hemimethylated DNA analog, depending on the sequence around the mCG/CG

8   [18,19], suggesting that the DNA Recognition Helix is intrinsically flexible; in contrast, our

9   DNMT1:H3Ub2:DNA$^{mCG/fCG}$ complex shows a rigid conformation of the DNA Recognition Helix,

10   indicating that the phenylalanine pair in the Activating Helix contributes to activation state of

11   DNMT1.

12

13   **Crucial role of a phenylalanine pair for activation of DNMT1**

14   The phenylalanines Phe631 and Phe632 are invariant between vertebrate species, and are

15   also present in the cephalochordate Amphioxus (Fig. 3f). We therefore asked whether these

16   residues played a role in the activation of DNMT1, as could be expected from the fact that they

17   bind the Toggle Pocket. In a binding assay, we found that the F631A/F632A mutations abolished

18   the ability of DNMT1 to bind hemimethylated DNA (Fig. 4a), even though the H3Ub2-binding

19   ability of DNMT1 was unaffected (Extended Data Fig. 1f). We carried out an *in vitro* DNA

20   methylation assay and, again, observed that the F631A/F632A mutation led to severe defects in

21   DNA methylation (Fig. 4b).

22   We then sought confirmation of these results in an *in vitro* assay, which reconstitutes

23   replication-coupled maintenance DNA methylation using *Xenopus* egg extracts [11,12,24]. In that

24   system, we immunodepleted DNMT1, and re-introduced recombinant DNMT1, either WT or

25   mutated on the 2 phenylalanines of the Activating Helix (F506A and F507A in *Xenopus*, FF/AA

26   mutant). As previously reported, the depletion of xDNMT1 from *Xenopus* egg extracts resulted in

27   the accumulation of chromatin-bound UHRF1 and ubiquitinated histone H3 species (Fig. 4c); this

28   is due to defective maintenance DNA methylation, which generates hemimethylated DNA from

29   which UHRF1 cannot be released [11,24]. The addition of wild-type (WT) recombinant xDNMT1

30   suppressed the accumulation of UHRF1 and ubiquitinated H3 (Fig. 4c). The FF/AA mutant

31   retained chromatin binding activity but failed to suppress the accumulation of UHRF1 and

1   ubiquitinated H3, showing defects in maintenance DNA methylation (Fig. 4c). Therefore, this

2   functional assay in *Xenopus* egg extracts further validated the effect of the mutation.

3   Lastly, we used a colon cancer cell line HCT116, in which DNA methylation has been

4   widely studied. In this line, both endogenous alleles of DNMT1 are tagged with an Auxin-

5   Inducible Degron (AID) (Fig. 4d). In this DNMT1-AID line, we introduced rescue vectors: one

6   encoding WT DNMT1, and the other encoding the FF/AA mutant (Fig. 4d). The level of

7   endogenous DNMT1, exogenous WT or FF/AA DNMT1 were comparable (Fig. 4e) and they were

8   located in nucleus (Extended Data Fig. 9). Treating the cells with indole-3-acetic acid (IAA)

9   caused the disappearance of endogenous DNMT1 but did not affect the exogenous proteins. We

10   then measured global DNA methylation at days 0, 4, and 8 after endogenous DNMT1 removal

11   (Fig. 4f). The control cells (empty vector) lost almost one-third of total DNA methylation, going

12   from 70% to 50% methylation. This loss was completely prevented by the WT DNMT1 transgene.

13   In contrast, the FF/AA DNMT1 mutant was incapable of sustaining DNA methylation

14   maintenance, and showed DNA methylation values close to those of the empty vector (Fig. 4f).

15   Collectively these experiments confirm that the Activating helix, and especially its

16   conserved phenylalanines, are crucial for DNA methylation maintenance by DNMT1.

17

Discussion

19   Our cryo-EM analysis reveals a molecular mechanism for human DNMT1 catalytic

20   activation (Fig. 5). Our results reveal both the large-scale displacements of inhibitory modules

21   (RFTS, CXXC, Auto-Inhibitory Linker), as well as more detailed changes, particularly the switch

22   by which the same hydrophobic pocket, initially bound to inhibitory phenylalanines, engages

23   activating phenylalanines, which releases the DNA Recognition Helix and permits catalysis. This

24   regulation also operates in *Xenopus*, and may even occur in invertebrates such as *Amphioxus*, in

25   which the regulatory amino acids are conserved (Fig. 3f). However, the process may be limited to

26   animals, as the Activating Helix containing the key phenylalanine is missing from the bacterial

27   methyltransferase M. HhaI (PDB: 1MHT) [25] or plant DNA methyltransferases such as maize

28   CMT3 homolog ZMET2 (PDB: 4FSX) [26] and Nicotiana tabacum DRM2 (PDB: 4ONJ) [27]. It would

29   be interesting for the future to determine which features of animal DNA methylation have

30   prompted the selection of this specific regulation for the maintenance DNA methyltransferase.

31   The catalytic domains of the *de novo* DNA methyltransferases DNMT3A and DNMT3B

32   bind the DNMT3L catalytic-like domain and form a heterotetramer [28–31]. Interestingly, the

1   DNMT3A(B)/3L interface is formed by hydrophobic interactions mediated by phenylalanine

2   residues, and therefore is known as the F-F interface. The F-F interface enhances DNA methylation

3   activity by the DNMT3A(B)/3L heterotetramer [28]. The hydrophobic residue in the DNMT3A(B)

4   catalytic domain spatially corresponds to the Toggle Pocket of DNMT1. Thus, covering the

5   hydrophobic pocket of the catalytic domain by an intra- or inter-molecule interaction could be an

6   evolutionarily conserved activation mechanism of DNA methyltransferases. The Activating Helix,

7   however, is unique to DNMT1 and crucial for enzymatic activation, and therefore could be utilized

8   to design novel inhibitors such as helical peptides that mimic this Activating Helix.

9   Previously reported structures of apo-DNMT1 and DNMT1:DNA$^{CG/CG}$ revealed a dual-

10   autoinhibitory mechanism in which the RFTS domain and the Auto-Inhibitory Linker are

11   embedded into the catalytic core, thereby inhibiting the access of cognate DNA (Fig. 5). Our cryo-

12   EM analysis of the ternary complex showed full dissociation of both the RFTS domain and Auto-

13   Inhibitory Linker from the catalytic core (Fig. 1b). Interestingly, H3Ub2-binding to the RFTS

14   domain might not be sufficient for displacement of the RFTS domain as our cryo-EM and SAXS

15   data showed that the C-lobe of RFTS domain is still accommodated in the catalytic core in the

16   DNMT1/H3Ub2 complex (Extended Data Fig. 5). A previous molecular dynamics simulation has

17   demonstrated that H3Ub2-binding reduces the contact number between the C-lobe and catalytic

18   core [12]. We hypothesize, therefore, that H3Ub2 binding destabilizes the inhibitory interaction

19   between the C-lobe and the catalytic core, allowing hemimethylated DNA to penetrate the catalytic

20   core. Thus, we propose that binding to H3Ub2 and DNA leads to full activation of DNMT1 via

21   the following structural changes: i) dissociation of the RFTS domain from the catalytic core, ii)

22   structural changes to a newly identified Activating Helix causing the conserved residues

23   Phe631/Phe632 to invade the Toggle Pocket of the catalytic domain, iii) adoption of a rigid

24   conformation by the DNA Recognition Helix, iv) spatial rearrangement of the CXXC domain and

25   v) eviction of the Auto-Inhibitory Linker from the catalytic domain (Fig. 5). Future work will

26   determine if these structural changes occur sequentially or simultaneously. Thus, our findings

27   describe new concepts and mechanisms in the multi-step activation process of DNMT1 that

28   ensures faithful maintenance of DNA methylation.
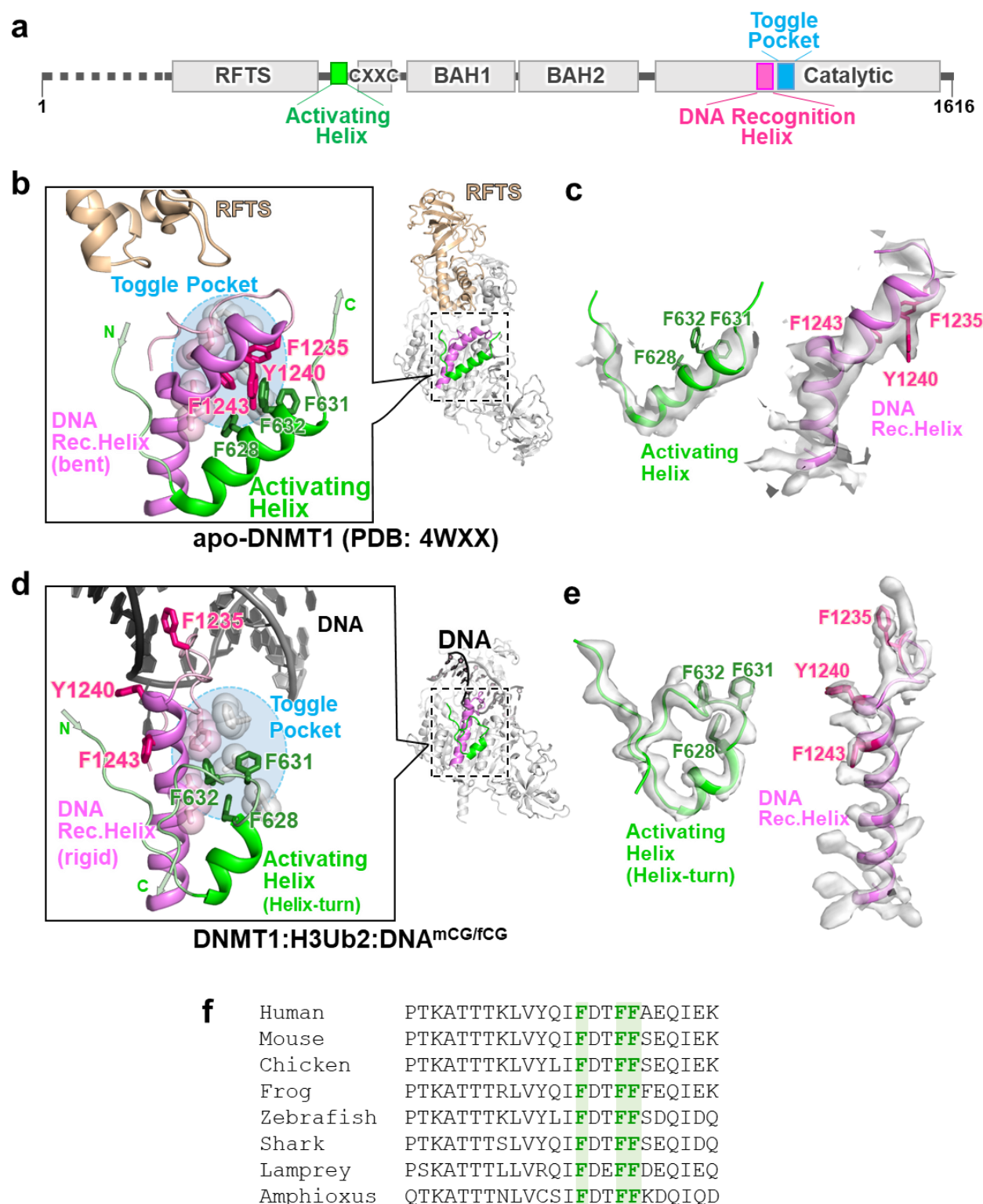
29

1 **Figure legends**
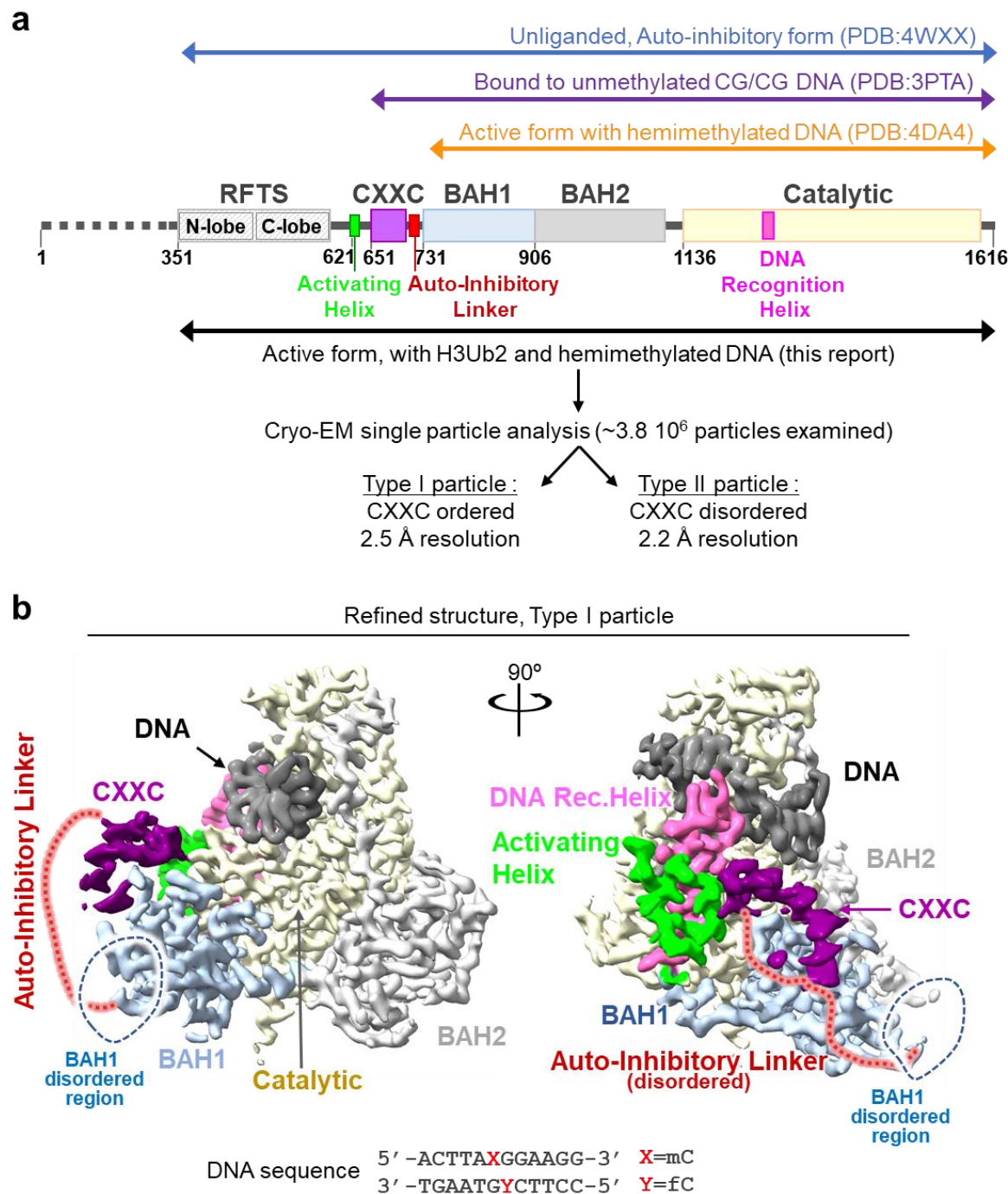
2 **Fig. 1. Cryo-EM single particle analysis of DNMT1:H3Ub2:DNA$^{\text{mCG/fCG}}$. a,** Domain

3 architecture of hDNMT1, with amino acid numbers indicated. **b,** Cryo-EM map of the

4 DNMT1:H3Ub2:DNA$^{\text{mCG/fCG}}$ ternary complex. Disordered Auto-Inhibitory Linker and N-terminal

5 portion of BAH1 domain are shown as dotted lines.

6
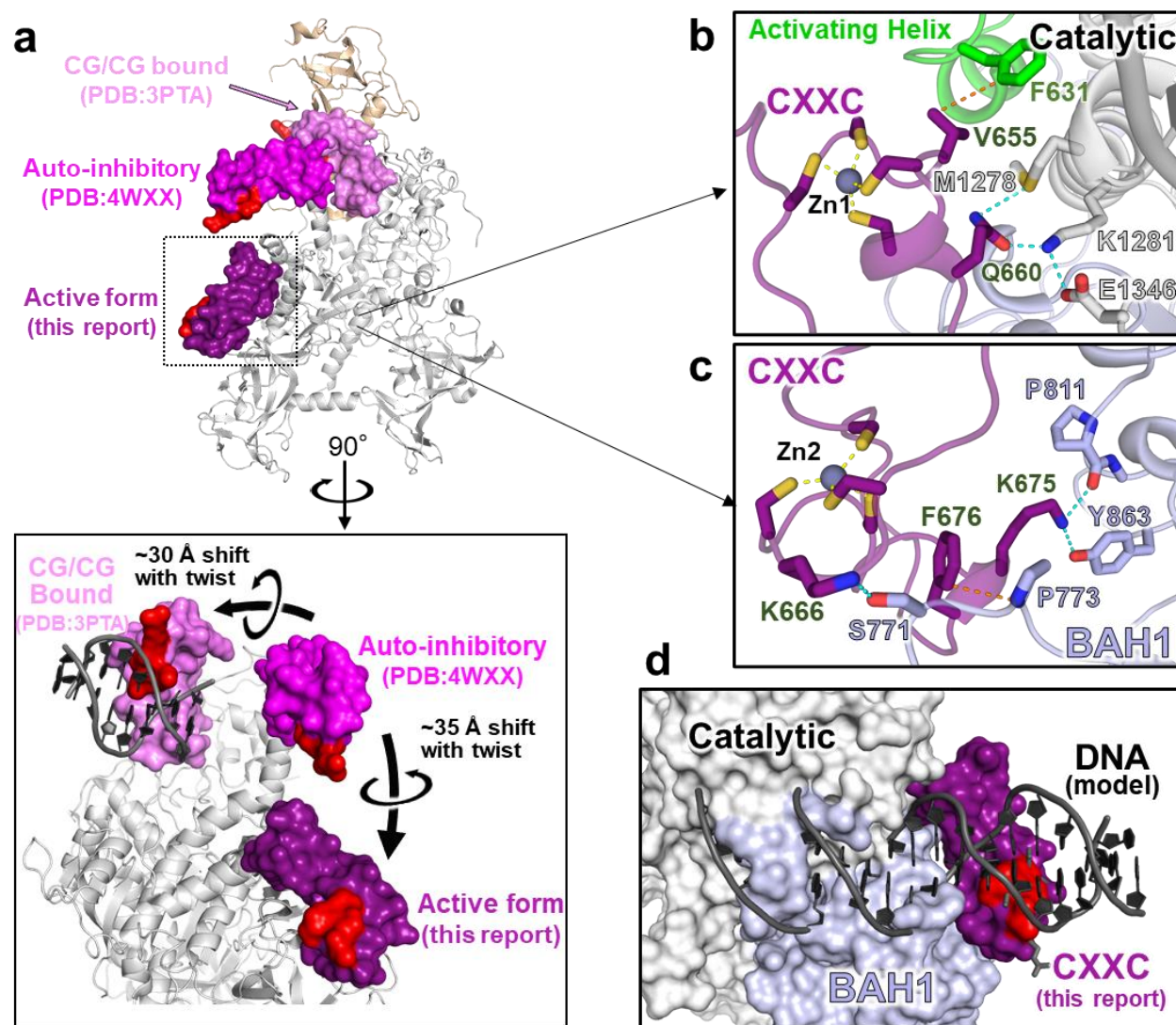
Fig. 2. Spatial rearrangement of the CXXC domain upon activation. a, Upper panel: comparison of CXXC domain position in the DNMT1:DNA$^{CG/CG}$ binary complex (PDB: 3PTA, light pink), in apo-DNMT1 (PDB:4WXX, medium pink), and in the ternary complex (dark pink). Each CXXC domain depicted as surface model is superimposed on the apo-DNMT1 structure shown as a cartoon model. The red surface in the CXXC domain indicates R681-K683, which bind the major groove of unmethylated DNA$^{CG/CG}$. Lower panel: close-up view showing the different spatial arrangements of the CXXC domain. **b,** Detail of the interaction between CXXC domain and catalytic domain showing gray cartoon and stick models in the ternary complex. **c,** Detail of the interaction between CXXC domain and BAH1 domain showing light-purple cartoon and stick models in the ternary complex. **d,** Model structure of CXXC domain bound to DNA$^{CG/CG}$ in the

1   ternary complex. CXXC:DNA$^{CG/CG}$ in PDB:3PTA is superimposed on the CXXC domain in the

2   ternary complex.

3

4

f

Human	PTKATTTKLVYQI**F**DT**FF**AEQIEK
Mouse	PTKATTTKLVYQI**F**DT**FF**SEQIEK
Chicken	PTKATTTKLVYLI**F**DT**FF**SEQIEK
Frog	PTKATTTRLVYQI**F**DT**FF**FEQIEK
Zebrafish	PTKATTTKLVYLI**F**DT**FF**SDQIDQ
Shark	PTKATTTSLVYQI**F**DT**FF**SEQIDQ
Lamprey	PSKATTTLLVRQI**F**DE**FF**DEQIEQ
Amphioxus	QTKATTTNLVCSI**F**DT**FF**KDQIQD

Fig. 3. Activation of DNMT1 by a pair of phenylalanine residues in the Activating Helix. a, Domain structure of DNMT1. **b,** Structure around Activating Helix (green), catalytic loop and DNA Recognition Helix (pink) of apo-DNMT1 (PDB:4WXX). Residues in Activating Helix and

1   DNA Recognition Helix that are involved in binding to the Toggle Pocket are shown as green and

2   pink stick models, respectively. Residues for formation of the Toggle Pocket are shown as stick

3   with transparent sphere model. The Toggle Pocket is highlighted by a light blue circle. **c,** Cryo-

4   EM map of apo-DNMT1 (EMD-33299) superimposed on crystal structure of apo-DNMT1

5   (PDB:4WXX), showing the similarity of Activating Helix and DNA Recognition Helix in both

6   approaches. **d,** Structure around Activating Helix, catalytic loop, and DNA Recognition Helix of

7   the ternary complex. **e,** Structure of Activating Helix and DNA Recognition Helix of the ternary

8   complex superposed on cryo-EM map (EMD-33200). **f,** Multiple sequence alignment of DNMT1

9   around the Activating Helix. Phenylalanines 628, 631 and 632 are highlighted.

10

11
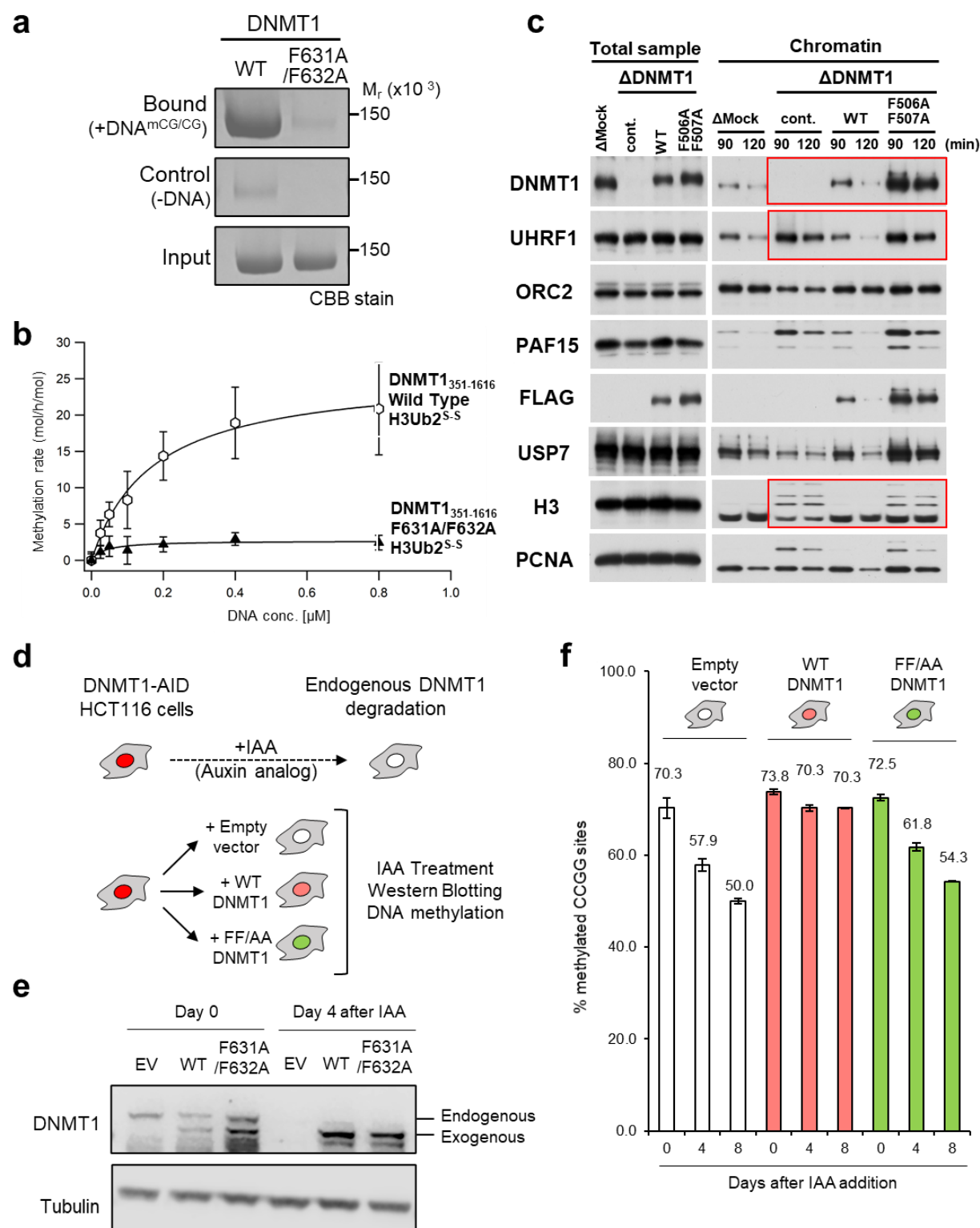
Fig. 4. Functional assays demonstrate the importance of the Activating Helix. a, Pull-down assay using immobilized hemimethylated DNA. **b,** *in vitro* DNA methylation activity of DNMT1 wild-type (white hexagons) and F631A/F632A mutant (blacks triangle) for hemimethylated DNA.

1   Vertical axis indicates the turnover frequency of the methylation reaction of DNMT1 (100 nM)

2   after one hour. Michaelis–Menten curve is shown as lines. **c,** *F* assay for DNA methylation

3   maintenance using *Xenopus* sperm chromatin and interphase egg extracts. WT DNMT1 is

4   functional in the assay, allowing for the release of UHRF1. The FF/AA mutant binds chromatin

5   but does not lead to UHRF1 release, showing that it cannot promote DNA methylation

6   maintenance. **d,** Experimental scheme in human HCT116 colon cancer cells: the endogenous

7   DNMT1 protein is tagged with an Auxin-Inducible Degron (AID) tag, causing the protein to be

8   degraded after addition of the auxin analog IAA. In this background, rescue vectors are added that

9   encode either WT or FF/AA versions of DNMT1. The empty Vector is used as a negative control.

10   **e,** Western blotting shows that endogenous DNMT1 is degraded upon IAA addition, whereas

11   exogenous WT and FF/AA DNMT1 are not degraded. **f,** Measurement of global DNA levels by

12   Luminometric Methylation Assay (LUMA). Cells expressing WT DNMT1 maintain global DNA

13   methylation when endogenous DNMT1 is degraded, whereas the FF/AA mutant does not support

14   DNA methylation maintenance.

15

16
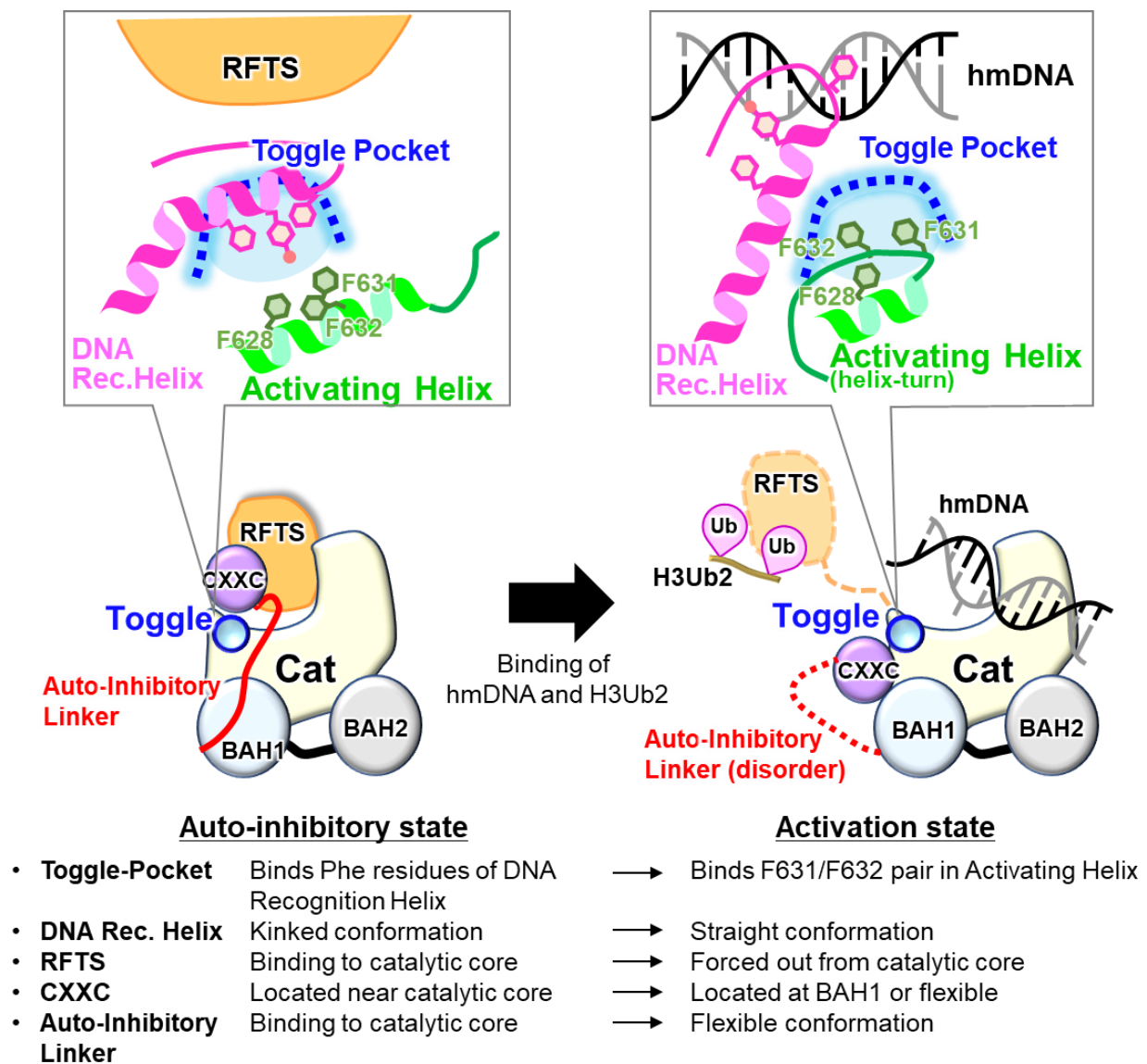
Fig. 5. Schematic representation of the DNMT1 activation mechanism. Left and right Figures show the auto-inhibitory and activation state of DNMT1, respectively.

Methods

Oligonucleotides

12 base of oligonucleotides (upper: 5'-ACTTA(5mC)GGAAGG, lower: 5'-CCTTC(5fC)GTAAGT) for cryo-EM single particle analysis, 42 base of oligonucleotides (upper: 5'-GGACATC(5mC)GTGAGATCGGAGGC(5mC)GCCTGCTGCAATC(5mC)GGTAG, lower: 5'-CTACCGGATTGCAGCAGGCGGCCTCCGATCTCACGGATGTCC) for DNA methylation assay and 21 base of oligonucleotides (upper: 5'-CAGGCAATC(5mC)GGTAGATCGCA, lower: 5'-biotin-TTGCGATCTACCGGATTGCCTG) for DNA pull-down assay were synthesized by GeneDesign, *Inc*. (Osaka, Japan). 5mC and 5fC mean 5-methylcytosine and 5-fluorocytosine, respectively. To prepare DNA duplex, the mixture of equimolar of complementary oligonucleotides were heated at 95 ℃ for 2 min and annealed at 4 ℃ for overnight.

Protein expression and purification

The gene encoding wild type and mutant of human DNMT1 (residues 351-1616) containing N-terminal ten histidine tag (His-tag) and human rhinovirus 3C (HRV 3C) protease site was amplified by PCR and cloned into the pFastBac vector (Invitrogen) using seamless cloning method. Baculoviruses for expression of the DNMT1 were generated in *Spodoptera frugiperda* 9 (Sf9) cells according to the Bac-to-Bac system instruction (Invitrogen). The protein expression was performed by infection of the baculoviruses with the Sf9 cells for 72 hrs at 27 ℃. Cells cultured with 1 L medium were lysed by lysis buffer (50 mM Tris-HCl [pH 8.0] containing 500 mM NaCl, 25 mM Imidazole, 10% Glycerol and 1mM DTT) and sonicated with the cycle of pulse on for 10 sec and pulse off for 50 sec (total pulse on time: 6 min). A soluble fraction was obtained after centrifugation of the lysate at 19,000 rpm for 40 min at 4 ℃ performed using Avanti J-E with a rotor JA-20 (BECKMAN COULTER) to remove insoluble debris.

The His-tagged DNMT1 was loaded to Ni-Sepharose 6 Fast Flow (Cytiva, Cat# 17531802), and unbound proteins were washed by wash buffer (50 mM Tris-HCl [pH 8.0] containing 1 M NaCl, 25 mM Imidazole, 10% Glycerol and 1 mM DTT), and lysis buffer. Bound proteins were eluted by an elution buffer (20 mM Tris-HCl [pH 8.0] containing 500 mM Imidazole, 300 mM NaCl, 10% Glycerol and 1 mM DTT). The His-tag was cleaved by the HRV3C protease at 4 ℃ for over 12 hrs. The DNMT1 was separated by anion-exchange chromatography, HiTrap Q HP (Cytiva, Cat# 17115401) using gradient elution from 50 to 1000 mM NaCl in 20 mM Tris-HCl [pH 8.0] buffer containing 10% Glycerol and 1 mM DTT. At the final stage, the DNMT1 was

1 purified with Hiload 26/600 Superdex 200 size exclusion chromatography (Cytiva, Cat#

2 28989336) equilibrated with 20 mM Tris-HCl [pH 7.5], 250 mM NaCl, 10% Glycerol and 5 mM

3 DTT.

4

5 **Preparation of disulfide- and isopeptide-linked ubiquitinated H3**

6 Disulfide-linked ubiquitinated H3 analog for SEC-SAXS and *in vitro* DNA methylation

7 assay was prepared using G76C mutant of ubiquitin (Ub-G76C) and K18C/K23C mutant of H3

8 peptide (residues 1-36 with an additional tryptophan residue at their C-terminus, hereafter $H3_{1-37W}$-K18C/K23C). Expression in *E. coli* and purification of the Ub-G76C and $H3_{1-37W}$ were

9 $_{37W}$-K18C/K23C). Expression in *E. coli* and purification of the Ub-G76C and $H3_{1-37W}$ were

10 purified according to the previous report [12]. After purification, these proteins were lyophilized.

11 The lyophilized Ub-G76C was dissolved in 50 mM sodium phosphate (pH 7.5) and mixed with a

12 20-fold molar excess of 5,5′-dithiobis-(2-nitrobenzoic acid) (DTNB, Wako) and the mixture was

13 incubated for 40 minutes at room temperature with rotation on a ROTATOR RT-5 (TITEC). The

14 reaction solution was buffer-exchanged into ligation buffer (20 mM Tris-HCl (pH 7.0), 50 mM

15 NaCl and 1 mM EDTA) using a PD-10 desalting column (Cytiva). Lyophilized $H3_{1-37W}$-

16 K18C/K23C was reduced in 20 mM Tris-HCl (H 7.5) containing 5 mM DTT, and were buffer-

17 exchanged into ligation buffer, and mixed with a 5-fold molar excess of activated Ub-G76C-

18 DTNB for 1 hr. The reaction product was purified on a cation-exchange column, Mono-S (Cytive).

19 Isopeptide-linked ubiquitinated H3 for cryo-EM single particle analysis was prepared

20 using mouse UBA1 (E1), human UBE2D3 (E2), human UHRF1 (E3), ubiquitin and $H3_{1-37W}$

21 harboring K14R/K27R/K36R mutations ($H3_{1-37W}$ K14R/K27R/K36R), which were purified in

22 house as previous report [24]. The ubiquitination reaction mixture contained 0.2 μM E1, 0.8 μM E2,

23 3 μM E3, 150 μM ubiquitin, and 50 μM $H3_{1-37W}$ K14R/K27R/K36R mutant in 1 mL of

24 ubiquitination reaction buffer (50 mM Tris-HCl (pH 8.5), 250 mM NaCl, 5 mM $MgCl_2$, 0.1%

25 Triton X-100, and 2 mM DTT). The reaction mixture was incubated at 30 °C for 6 h, and thereafter

26 the reaction was quenched by the heat shock at 70 °C for 30 min, followed by collecting soluble

27 fraction (Extended Data Fig. 1a). 6 μM of 18bp hemimethylated DNA was added in initially

28 ubiquitination reaction to enhance the ubiquitination reaction, however, the DNA addition was

29 omitted for the sample preparation of DNMT1:H3Ub2:DNA$^{mCG/fCG}$ to prevent DNA

30 contamination.

31

32 **Preparation of binary and ternary complex for cryo-EM single particle analysis**

1   For preparation of DNMT1:H3ub2 binary complex, 20 µM isopeptide bound-ubiquitinated

2   H3$_{1-37}$ mixed with 6.6 µM apo-DNMT1 was subjected to size excursion chromatography

3   (Superdex® 200 Increase 10/300 GL, Cytiva) equilibrated with the buffer (20 mM Tris-HCl [pH

4   7.5], 250 mM NaCl, 10 µM Zn(OAc)$_2$, and 0.5 mM DTT).

5   For preparation of ternary complex, purified DNMT1-H3Ub2 was mixed with 12 base pair

6   of hemimetylated DNA analog (upper: 5'-ACTTA(5mC)GGAAGG, lower: 5'-

7   CCTTC(5fC)GTAAGT: DNA$^{mCG/fCG}$) in the conjugation buffer (50 mM Tris-HCl [pH 7.5], 20%

8   Glycerol, 5 mM DTT and 50 mM NaCl). The conjugation reaction was initiated by the adding of

9   500 µM S-adenosyl-L-methionine (SAM) at 25°C for 4 hrs. The yield was purified by size

10 exclusion chromatography (Superdex® 200 Increase 10/300 GL, Cytiva) equilibrated with cryo-

11 EM buffer (20 mM Tris-HCl [pH 7.5], 250 mM NaCl and 5 mM DTT).

12

13 **Cryo-EM data collection**

14 A 3 µL of the protein solutions was applied onto the glow-discharged holey carbon grids

15 (Quantifoil Cu R1.2/1.3, 300 mesh). The grids were plunge-frozen in liquid ethane using a Vitrobot

16 Mark IV (Thermo Fisher Scientific). Parameters for plunge-freezing were set as follows: blotting

17 time, 3 sec; waiting time, 3 sec; blotting force, -10; humidity, 100%; and chamber temperature,

18 4 °C. Data for DNMT1:H3Ub2:DNA$^{mCG/fCG}$ ternary complex was collected at the University of

19 Tokyo on a 300-kV Titan Krios electron microscope (Thermo Fisher Scientific) with a K3 direct

20 electron detector (Gatan) with BioQuantum energy filter in counting mode. A total of 4,068 movies

21 were recorded at nominal magnification of ×105,000 and a pixel size of 0.83 Å/pixel, with a

22 defocus range between -0.8 and -1.8 µm and a dose rate of 1.25 electrons/Å^2 per frame. A typical

23 motion-corrected cryo-EM image is shown in Supplementary Fig. 1a.

24 Data of apo-DNMT1, DNMT1:H3Ub2 were collected at RIKEN BDR on a 200-kV Tecnai

25 Arctica electron microscope (Thermo Fisher Scientific) with a K2 direct electron detector (Gatan)

26 in counting mode. A total 2,071 movies for apo-DNMT1 and 1,869 movies for DNMT1:H3Ub2

27 were recorded at nominal magnification of ×23,500 and a pixel size of 1.477 Å/pixel, with a

28 defocus range between -0.8 and -1.4 µm, and a dose rate of 1.25 electrons/Å^2 per frame. A typical

29 motion-corrected cryo-EM image is shown in Supplementary Figs. 2a and 3b.

30

31 **Data processing**

1   All Data were processed using cryoSPARC v3.2.0 [32] for PDB deposition. The movie stacks

2   were motion corrected by Full-frame motion correction or Patch motion correction. The defocus

3   values were estimated from Contrast transfer function (CTF) by Patch CTF estimation or

4   CTFFIND4 [33]. A total of 4,307,107 particles of DNMT1:H3Ub2:DNA$^{mCG/fCG}$ ternary complex

5   were automatically picked using blob picker with 80 Å, 105 Å and 130 Å circular blobs and 80-

6   130 Å elliptical blobs (Supplementary Fig. 1b). Particles (3,798,046) were then extracted in a box

7   size of 256 pixels with a 0.83 Å/pixel size followed by single round of reference-free 2D

8   classifications (Supplementary Fig. 1c). The selected good class containing 1,621,988 particles

9   were used for *ab initio* 3D reconstruction (Extended Date Fig. 3). Then, non-uniform refinement

10   was performed against all the extracted particles to yield the cryo-EM map with an overall

11   resolution of 2.09 Å resolution. The subsequent heterogeneous refinement selected 2,653,627

12   particles as a good class. These particles were subjected to a 3D variability analysis, separating the

13   CXXX-ordered and CXXC-disordered models. The particles (138,662) in the CXXC-ordered

14   model and those (897,446) in the CXXC-disordered models were then subjected to non-uniform

15   refinement to generate a cryo-EM map with an overall resolution of 2.52 Å and 2.23 Å,

16   respectively. The classification processes were shown in Extended Data Fig. 3, and the statics of

17   data collection and refinement and validation were shown in Table 1.

18   A total of 3,984,637 particles of apo-DNMT1 were automatically picked using blob picker

19   with 80 Å, 105 Å and 130 Å circular blobs (Supplementary Fig. 2b). Particles (3,984,637) were

20   then extracted in a box size of 160 pixels with a 1.477 Å/pixel size, followed by two rounds of

21   reference-free 2D classifications to remove junk particles (Supplementary Fig. 2c). The selected

22   3,666,067 particles were subjected for *ab initio* 3D model reconstruction to generate four cryo-

23   EM maps (Supplementary Fig. 4). An initial model shows similar shape with the crystal structure

24   of DNMT1 (PDB: 4WXX). Then, non-uniform refinement was performed against the particles

25   classified in the initial model of DNMT1 (1,824,727). These particles were re-extracted in a box

26   size of 256 pixels with a 1.477 Å/pixel size by local motion correction. Non-uniform refinement

27   yields the cryo-EM map with an overall resolution of 3.32 Å resolution. These particles were

28   subjected to a 3D variability analysis and heterogeneous refinement, removing the dimer particles,

29   and separating RFTS-free map and RFTS-bound map. To improve the cryo-EM map, further 3D

30   variability analysis and clustering by PCA was performed. The particles (380,989) were then

31   subjected to non-uniform refinement to yield final cryo-EM map. Overall resolution of 3.45 Å

32   resolution using the gold-standard Fourier shell correlation with a 0.143 cut-off. The classification

1   processes were shown in Supplementary Fig. 4, and the statics of data collection and refinement

2   and validation were shown in Supplementary Table 1.

3   A total of 2,463,410 particles of DNMT1:H3Ub2 were automatically picked using blob

4   picker with 80 Å, 105 Å and 130 Å circular blobs (Supplementary Fig. 3b). The particles were

5   then extracted in a box size of 160 pixels in a 1.477 Å/pixel size using cryoSPARC followed by

6   initial dataset cleanup using reference-free 2D classifications (Supplementary Fig. 3c). The

7   selected 2,336,267 particles were subjected for *ab initio* 3D model reconstruction to generate four

8   cryo-EM maps (Supplementary Fig. 5). Further 2D classifications were performed by the 2 class

9   of *ab initio* 3D model assigned as DNMT1 particles. The particles (160,088) belong with the best

10   four 2D classes were subjected to create the fine initial model. For the further refinement, the

11   particles (1,303,645) without ice images from 2D classification II were selected. These particles

12   were re-extracted in a box size of 256 pixels with a 1.477 Å/pixel size by local motion correction.

13   Non-uniform refinement yields the cryo-EM map with an overall resolution of 3.55 Å resolution.

14   These particles were subjected to a 3D variability analysis and heterogeneous refinement,

15   separating RFTS-free map and RFTS-bound map. The subsequent 2D classification selected

16   735,233 particles as RFTS-bound structure. To improve the cryo-EM map, further 3D variability

17   analysis and clustering by PCA was performed. The particles (645,368) were then subjected to

18   non-uniform refinement to yield final cryo-EM map. Overall resolution of 3.52 Å resolution using

19   the gold-standard Fourier shell correlation with a 0.143 cut-off. The classification processes were

20   shown in Supplementary Fig. 5, and the statics of data collection and refinement and validation

21   were shown in Supplementary Table 1.

22   For the analysis of H3Ub2-RFTS domain complex, the 2D classification analysis were also

23   performed by Relion 3.1 (Extended Data Fig. 6) [34]. The movie stacks of

24   DNMT1:H3Ub2:DNAmCG/fCG were motion corrected by MotionCor2. The defocus values were

25   estimated from Contrast transfer function (CTF) by CTFFIND4 [33].Single particle image was also

26   extracted by LoG Auto picker of Relion to check the particles of other biomolecules. After three

27   rounds of 2D classification, the particle smaller than DNMT1 was selected. These smaller particles

28   (80,186) were re-extracted in a box size of 128 pixels with a 0.83 Å/pixel size, and the images

29   were classified by 2D classification. The major 2D average images were compared with the

30   projected templates of RFTS-H3Ub2 complex (PDB: 5WVO) (Extended Data Fig. 6). Gaussian

31   model of the complex was created by the Molmap of ChimeraX [35]. The 2D projected templates

32   were created by the module of "create template" in cryoSPARC.

1

SEC-SAXS

SAXS data were collected on Photon Factory BL-10C using a HPLC Nexera/Prominence-I (Shimazu) integrated SAXS set-up. 100 µl of a 10 mg/ml of the apo-DNMT1 (aa:351-1616) or its bound to H3Ub2^{S-S} were loaded onto a Superdex® 200 Increase 10/300 GL (Cytive) pre-equilibrated with 20 mM Tris-HCl (pH 8.0), 150 mM NaCl and 5% glycerol at a flow rate of 0.5 ml/min at 20 °C. The flow rate was reduced to 0.05 ml/min at an elution volume of 10 -13 ml. X-ray scattering was collected every 20 seconds on a PILATUS3 2M detector over an angular range of $q_{min} = 0.00690$ Å^{-1} to $q_{max} = 0.27815$ Å^{-1}. UV spectra at a range of 200 nm to 450 nm were recorded every 10 seconds. Circular averaging and buffer subtraction were carried out using the program SAngler [36] to obtain one-dimensional scattering data $I(q)$ as a function of q ($q = 4\pi\sin\theta/\lambda$, where 2θ is the scattering angle and λ is the X-ray wavelength 1.5 Å). The scattering intensity was normalized on an absolute scale using the scattering intensity of water [37]. The multiple concentrations of the scattering data around the peak at A280, namely ascending and descending parts of chromatography peak, and $I(0)$ were extrapolated to zero-concentration by Serial Analyzer [38]. The molecular mass of the measured proteins was estimated by the empirical volume of correlation, V_c, showing no aggregation of the measured sample [39]. The radius of gyration R_g and the forward scattering intensity $I(0)$ were estimated from the Guinier plot of $I(q)$ in the smaller angle region of $qR_g < 1.3$. The distance distribution function $P(r)$ was calculated using the program GNOM [40]. The maximum particle dimension D_{max} was estimated from the $P(r)$ function as the distance r for which $P(r) = 0$. The scattering profile of crystal structure of apo-DNMT1 and its docking model with ubiquitinated H3 were computed with CRYSOL [41].

In vitro DNA methylation assay

The 42 base pair of DNA duplex containing three hemimethylation sites (1.6 µM) was methylated with the recombinant DNMT1 (15 nM, aa:351-1616) by the addition of the disulfide-linked ubiquitinated H3 (0 - 4 µM H3Ub2^{S-S}) including 20 µM SAM in reaction buffer (20 mM Tris-HCl [pH 8.0], 50 mM NaCl, 1 mM EDTA, 3 mM MgCl$_2$, 0.1 mg/mL BSA and 20% Glycerol) at 37 ℃ for 1 hr. Termination of methylation reaction and conversion of SAH to ADP were performed by the addition of 5×MTase-Glo^{TM} reagent from methyltransferase assay kit, MTase-Glo (Promega) at 1:4 ratio for the reaction total volume. After 30 min stationary at room temperature, ADP detection process was carried out with solid white flat bottom 96 well plates

1   (Costar). MTase-Glo^{TM} Detection Solution was added to the reaction in 1:1 ratio to reaction total

2   40 µl volume and incubated for 30 min at room temperature. The luminescence derived from

3   reaction product, SAH, was monitored using GloMax® Navigator Microplate Luminometer

4   (Promega). The effect of F631A/F632A mutation were examined at the condition of the DNMT1

5   (15 nM) with 2 µM H3Ub2^{S-S} by the addition of 42 base pair of DNA duplex (0 - 0.8 µM) in same

6   reaction buffer. The SAH conversion process and ADP detection process in the manner described

7   above.

8   For the evaluation of the DNMT1:H3Ub2 complex, final concentration of DNMT1 was 50

9   nM to prevent the dissociation of ubiquitinated H3 (K_D = 18 nM). DNA methylation reactions were

10 initiated by mixing of apo-DNMT1 or DNMT1:H3Ub2^{iso} and the stopped at 0, 5, 15 or 30 min by

11 addition of 5×MTase-Glo^{TM} reagent. The detection process was performed in the same way as

12 described above. At least three independent experiments were performed for estimation of standard

13 deviation.

14

15 *DNA pull-down assay*

16   20 µg of the 21 base pair of biotinylated hemimethylated DNA duplex was immobilized

17 on Dynabeads M-280 Streptavidin (VERITAS) equilibrated with the binding buffer (20 mM Tris-

18 HCl [pH 7.5], 150 mM NaCl, 10% Glycerol and 0.05% NP-40). After washing the beads with the

19 binding buffer, 10 µg of purified DNMT1 (aa:351-1616) wild-type or F631A/F632A mutant, 2-

20 equimolar excess of H3Ub2^{S-S} and equimolar of SAH were added to the beads. After incubation

21 for 2 hr at 4 ℃, the unbound proteins were washed five times with the binding buffer. The proteins

22 bound to the immobilized DNA were boiled for 2 min at 95 ℃ in an oxidative SDS-loading buffer

23 and analyzed by SDS-PAGE using SuperSep^{TM} Ace, 5-20% gel (Wako, Japan). At least three

24 independent experiments were performed.

25

26 **Cell Culture, Transfection, and Colony Isolation**

27   The HCT116 cell line, which conditionally expressed OsTIR1 under the control of a

28 tetracycline (Tet)-inducible promoter, was obtained from the RIKEN BRC Cell Bank

29 (http://cell.brc.riken.jp/en/), and genotyped by Eurofins. All cell lines were cultured in McCoy's

30 5A medium (Sigma-Aldrich) supplemented with 10% FBS (Gibco), 2 mM L-glutamine, 100 U/mL

31 penicillin, and 100 µg/mL streptomycin. Cells were grown in a 37 ℃ humid incubator with 5%

32 CO_2. To generate stable DNMT1-AID cell lines, we followed previous studies [42,43]. Briefly, cells

1   were grown in a 24 well plate, then CRISPR/Cas and donor plasmids were transfected using

2   Lipofectamine 2000 (Thermo Fisher Scientific). Two days after transfection, cells were transferred

3   and diluted in 10-cm dishes, followed by selection in the presence of 700 mg/ml G418 or 100

4   mg/ml Hygromycin B. After 10–12 days, colonies were picked for further selection in a 96-well

5   plate. To induce the degradation of AID-fused proteins, cells were incubated with 0.2 µg/mL

6   doxycycline (Dox) and 20 µM auxinole for 1 day, then we replaced the medium including 0.2

7   µg/mL Dox and 500 µM indole-3-acetic acid (IAA), a natural auxin.

8

9   **Establishment of stable expressing exogenous DNMT1 cell lines for rescue experiments**

10   We cloned WT DNMT1 and point mutant DNMT1 (F631A/F632A) to pSBbi-Bla

11   (Addgene: 60526). All plasmids were sequenced prior to use. To establish stable expressing

12   exogenous DNMT1 cell lines, we used sleeping beauty system[44]. Briefly, cells were grown in a 6

13   well plate, then transposase vector (Addgene: 34879) and each pSBbi-Bla plasmids (EV, WT,

14   F631A/F632A) were transfected using Lipofectamine 2000 (Thermo Fisher Scientific). Four days

15   after transfection, cells were selected with 10 µg/mL Blasticidin for one week. To detect DNA

16   methylation level, LUMA and Pyrosequencing were done according to standard procedures.

17

18   **Data availability**

19   The cryo-EM density map has been deposited in the Electron Microscopy Data Bank

20   (EMDB, www.ebi.ac.uk/pdbe/emdb/) with the accession code EMD-33200, EMD-33201, EMD-

21   33298, EMD-33299 and the atomic coordinates have been deposited in the PDB (www.rcsb.org)

22   with the accession code 7XI9, 7XIB. All data needed to evaluate the conclusions in the paper are

23   present in the paper and/or the Supplementary Materials. Additional data related to this paper may

24   be requested from the authors.

25

26   **References**

27   1.   Greenberg, M. V. C. & Bourc'his, D. The diverse roles of DNA methylation in mammalian

28   development and disease. *Nature reviews. Molecular cell biology* **20**, 590–607 (2019).

29   2.   Schübeler, D. Function and information content of DNA methylation. *Nature* **517**, 321–326

30   (2015).

3. Nishiyama, A. & Nakanishi, M. Navigating the DNA methylation landscape of cancer. *Trends in Genetics* **37**, 1012–1027 (2021).

4. Petryk, N., Bultmann, S., Bartke, T. & Defossez, P. A. Staying true to yourself: mechanisms of DNA methylation maintenance in mammals. *Nucleic acids research* **49**, 3020–3032 (2021).

5. Bostick, M. *et al.* UHRF1 plays a role in maintaining DNA methylation in mammalian cells. *Science (New York, N.Y.)* **317**, 1760–1764 (2007).

6. Sharif, J. *et al.* The SRA protein Np95 mediates epigenetic inheritance by recruiting Dnmt1 to methylated DNA. *Nature* **450**, 908–912 (2007).

7. Arita, K., Ariyoshi, M., Tochio, H., Nakamura, Y. & Shirakawa, M. Recognition of hemi-methylated DNA by the SRA protein UHRF1 by a base-flipping mechanism. *Nature* **455**, 818–821 (2008).

8. Hashimoto, H. *et al.* The SRA domain of UHRF1 flips 5-methylcytosine out of the DNA helix. *Nature* **455**, 826–829 (2008).

9. Avvakumov, G. V *et al.* Structural basis for recognition of hemi-methylated DNA by the SRA domain of human UHRF1. *Nature* **455**, 822–825 (2008).

10. Qin, W. *et al.* DNA methylation requires a DNMT1 ubiquitin interacting motif (UIM) and histone ubiquitination. *Cell research* **25**, 911–29 (2015).

11. Nishiyama, A. *et al.* Uhrf1-dependent H3K23 ubiquitylation couples maintenance DNA methylation and replication. *Nature* **502**, 249–53 (2013).

12. Ishiyama, S. *et al.* Structure of the Dnmt1 Reader Module Complexed with a Unique Two-Mono-Ubiquitin Mark on Histone H3 Reveals the Basis for DNA Methylation Maintenance. *Molecular Cell* **68**, 350-360.e7 (2017).

13. Ren, W. *et al.* Direct readout of heterochromatic H3K9me3 regulates DNMT1-mediated maintenance DNA methylation. *Proceedings of the National Academy of Sciences of the United States of America* **117**, 18439–18447 (2020).

14. Karg, E. *et al.* Ubiquitome Analysis Reveals PCNA-Associated Factor 15 (PAF15) as a Specific Ubiquitination Target of UHRF1 in Embryonic Stem Cells. *Journal of molecular biology* **429**, 3814–3824 (2017).

15. Ren, W., Gao, L. & Song, J. Structural Basis of DNMT1 and DNMT3A-Mediated DNA Methylation. *Genes* **9**, (2018).

16. Zhang, Z. M. *et al.* Crystal Structure of Human DNA Methyltransferase 1. *Journal of molecular biology* **427**, 2520–2531 (2015).

17. Takeshita, K. *et al.* Structural insight into maintenance methylation by mouse DNA methyltransferase 1 (Dnmt1). *Proceedings of the National Academy of Sciences of the United States of America* **108**, 9055–9059 (2011).

18. Song, J., Teplova, M., Ishibe-Murakami, S. & Patel, D. J. Structure-based mechanistic insights into DNMT1-mediated maintenance DNA methylation. *Science* **335**, 709–712 (2012).

19. Adam, S. *et al.* DNA sequence-dependent activity and base flipping mechanisms of DNMT1 regulate genome-wide DNA methylation. *Nature Communications 2020 11:1* **11**, 1–15 (2020).

20. Pappalardi, M. B. *et al.* Discovery of a first-in-class reversible DNMT1-selective inhibitor with improved tolerability and efficacy in acute myeloid leukemia. *Nature Cancer 2021 2:10* **2**, 1002–1017 (2021).

21. Osterman, D. G., Depillis, G. D., Wu, J. C., Matsuda, A. & Santi, D. V. 5-Fluorocytosine in DNA is a mechanism-based inhibitor of HhaI methylase. *Biochemistry* **27**, 5204–5210 (1988).

22. Punjani, A. & Fleet, D. J. 3D variability analysis: Resolving continuous flexibility and discrete heterogeneity from single particle cryo-EM. *Journal of structural biology* **213**, (2021).

23. Song, J., Rechkoblit, O., Bestor, T. H. & Patel, D. J. Structure of DNMT1-DNA complex reveals a role for autoinhibition in maintenance DNA methylation. *Science* **331**, 1036–1040 (2011).

24. Nishiyama, A. *et al.* Two distinct modes of DNMT1 recruitment ensure stable maintenance DNA methylation. *Nature Communications* **11**, 1222 (2020).

25. Klimasauskas, S., Kumar, S., Roberts, R. J. & Cheng, X. HhaI methyltransferase flips its target base out of the DNA helix. *Cell* **76**, 357–369 (1994).

26. Du, J. *et al.* Dual binding of chromomethylase domains to H3K9me2-containing nucleosomes directs DNA methylation in plants. *Cell* **151**, 167–180 (2012).

27. Zhong, X. *et al.* Molecular mechanism of action of plant DRM de novo DNA methyltransferases. *Cell* **157**, 1050–1060 (2014).

28. Jia, D., Jurkowska, R. Z., Zhang, X., Jeltsch, A. & Cheng, X. Structure of Dnmt3a bound to Dnmt3L suggests a model for de novo DNA methylation. *Nature* **449**, 248–251 (2007).

29. Lin, C. C., Chen, Y. P., Yang, W. Z., Shen, J. C. K. & Yuan, H. S. Structural insights into CpG-specific DNA methylation by human DNA methyltransferase 3B. *Nucleic acids research* **48**, 3949–3961 (2020).

30. Zhang, Z. M. *et al.* Structural basis for DNMT3A-mediated de novo DNA methylation. *Nature* **554**, 387–391 (2018).

31. Gao, L. *et al.* Comprehensive structure-function characterization of DNMT3B and DNMT3A reveals distinctive de novo DNA methylation mechanisms. *Nature Communications 2020 11:1* **11**, 1–14 (2020).

32. Punjani, A., Rubinstein, J. L., Fleet, D. J. & Brubaker, M. A. cryoSPARC: algorithms for rapid unsupervised cryo-EM structure determination. *Nature methods* **14**, 290–296 (2017).

33. Frauer, C. *et al.* Recognition of 5-hydroxymethylcytosine by the Uhrf1 SRA domain Supplementary Table S1 . Sequences of DNA oligonucleotides used for preparation of double stranded fluorescent DNA substrates .

34. Scheres, S. H. W. & IUCr. Amyloid structure determination in RELION-3.1. *urn:issn:2059-7983* **76**, 94–101 (2020).

35. Pettersen, E. F. *et al.* UCSF ChimeraX: Structure visualization for researchers, educators, and developers. *Protein science : a publication of the Protein Society* **30**, 70–82 (2021).

36. Shimizu, N. *et al.* Software development for analysis of small-angle x-ray scattering data. in *AIP Conference Proceedings* **1741**, 050017 (AIP Publishing LLC, 2016).

37. Orthaber, D., Bergmann, A. & Glatter, O. SAXS experiments on absolute scale with Kratky systems using water as a secondary standard. *Journal of Applied Crystallography* **33**, 218–225 (2000).

38. Yonezawa, K., Takahashi, M., Yatabe, K., Nagatani, Y. & Shimizu, N. Software for serial data analysis measured by SEC-SAXS/UV-Vis spectroscopy. in 060082 (2019). doi:10.1063/1.5084713

39. Rambo, R. P. & Tainer, J. A. Accurate assessment of mass, models and resolution by small-angle scattering. *Nature* **496**, 477–481 (2013).

40. Svergun, D. I. Restoring low resolution structure of biological macromolecules from solution scattering using simulated annealing. *Biophysical journal* **76**, 2879–86 (1999).

41. Svergun, D., Barberato, C. & Koch, M. H. CRYSOL – a Program to Evaluate X-ray Solution Scattering of Biological Macromolecules from Atomic Coordinates. *urn:issn:0021-8898* **28**, 768–773 (1995).

42. Yesbolatova, A., Natsume, T., Hayashi, K. ichiro & Kanemaki, M. T. Generation of conditional auxin-inducible degron (AID) cells and tight control of degron-fused proteins using the degradation inhibitor auxinole. *Methods (San Diego, Calif.)* **164**–**165**, 73–80 (2019).

43. Natsume, T., Kiyomitsu, T., Saga, Y. & Kanemaki, M. T. Rapid Protein Depletion in Human Cells by Auxin-Inducible Degron Tagging with Short Homology Donors. *Cell reports* **15**, 210–218 (2016).

44. Mátés, L. *et al.* Molecular evolution of a novel hyperactive Sleeping Beauty transposase enables robust stable gene transfer in vertebrates. *Nature genetics* **41**, 753–761 (2009).

Acknowledgments

7

Author information

9   These authors contributed equally: Hiroki Onoda, Amika Kikuchi

10

Contributions

12 K.A. supervised the work. H.O., A.K., S.K., S.M., S.Y., and H.S. performed cloning and protein

13 purification. H.O., A.K., S.Y., H.S. performed *in vitro* biochemical assay. S.K., and K.A.

14 performed SEC-SAXS experiments and analysis. H.O., A.K., A.Y., M.S., N.A., K.A. performed

15 Cryo-EM experiments and analysis. Y.C., S.T., M.N., and A.N. performed evaluation of mutant

16 using *Xenopus* egg extract and K.Y., J.S., H.K., and PAD performed cell-based assay. H.O., PAD,

17 and K.A. wrote the paper.

18

Corresponding author

20 Correspondence to Kyohei Arita

21

Competing interests

23 Authors declare that they have no competing interests.

24

Funding

8
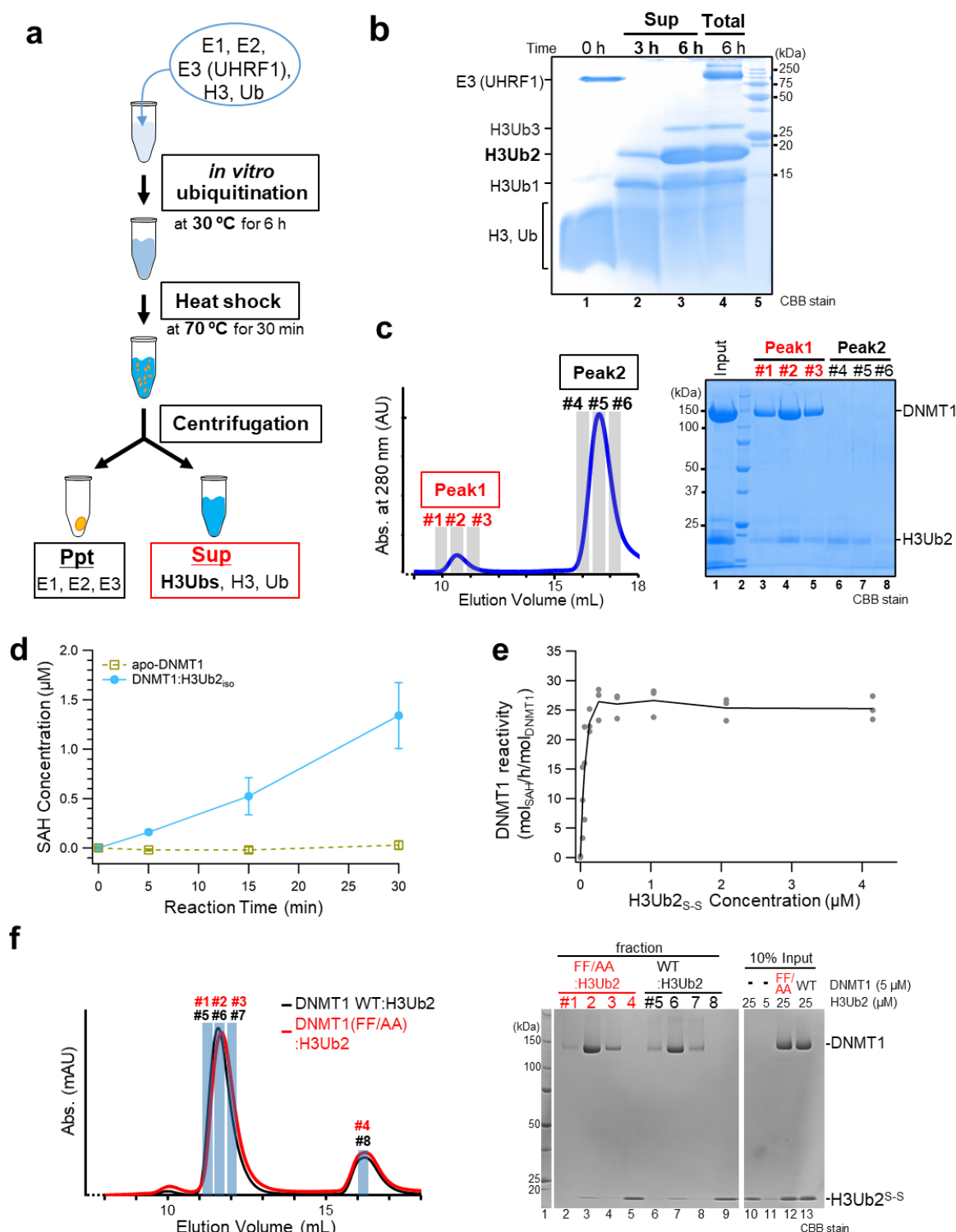
1   **Extended Data Fig. 1 Sample preparation of DNMT1:H3Ub2 and biochemical assay. (a)** Schematic figure of *in*

2   *vitro* preparation of ubiquitinated H3. **(b)** Analysis of ubiquitination of histone $H3_{1-37W}$ by SDS-PAGE. Lane 1: ATP

3   omitted-reaction cocktail, lanes 2 and 3: Supernatant (sup) of *in vitro* ubiquitination reaction cocktail for 3 hrs and 6

4   hrs after heat-shock at 70 °C, lanes 4: Total proteins in the reaction cocktail for 6 hrs reaction after the heat shock.

5   **(c)** Size exclusion chromatography of the mixture of $DNMT1_{351-1616}$ and excess ubiquitinated H3. Vertical and

32

1   horizontal axes indicate the absorbance of 280 nm (blue line) and elution volume of Superdex$^{®}$ 200 Increase 10/300

2   GL, respectively. SDS-PAGE of input (lane 1) and elution fractions (lane 3-8) at the Peak1 and 2 were depicted in

3   the chart of size exclusion chromatography. **(d)** DNA methylation assay of apo-DNMT1 (yellow-green) and its

4   complex with isopeptide bonded H3Ub2 including K14R/K27R/K36R mutations (cyan). The binary complex was

5   purified by size exclusion chromatography. At least three independent experiments were performed for estimation of

6   standard deviation. **(e)** DNA methylation assay of DNMT1 (aa:351-1616) in the absence of and presence of

7   H3Ub2^{S-S}. Vertical and horizontal axes indicate turnover frequency of DNA methylation (SAH concentration

8   divided by DNMT1 concentration after 1 hr reaction) and concentration of H3Ub2^{S-S}, respectively. Line shows the

9   average value of three times independent experiments. **(f)** Left: Size exclusion chromatography of the mixture of

10   DNMT1$_{351-1616}$ wild type (WT) or mutant (FF/AA: F631A/F632A) and excess H3Ub2^{S-S}. Vertical and horizontal

11   axes indicate the absorbances at 280 nm and elution volume of Superdex$^{®}$ 200 Increase 10/300 GL, respectively.

12   Right: Analysis of complex formation of DNMT1 WT or FF/AA mutant and H3Ub2^{S-S} by SDS-PAGE. Lanes 10-13

13   show the input sample for the SEC analysis.

14
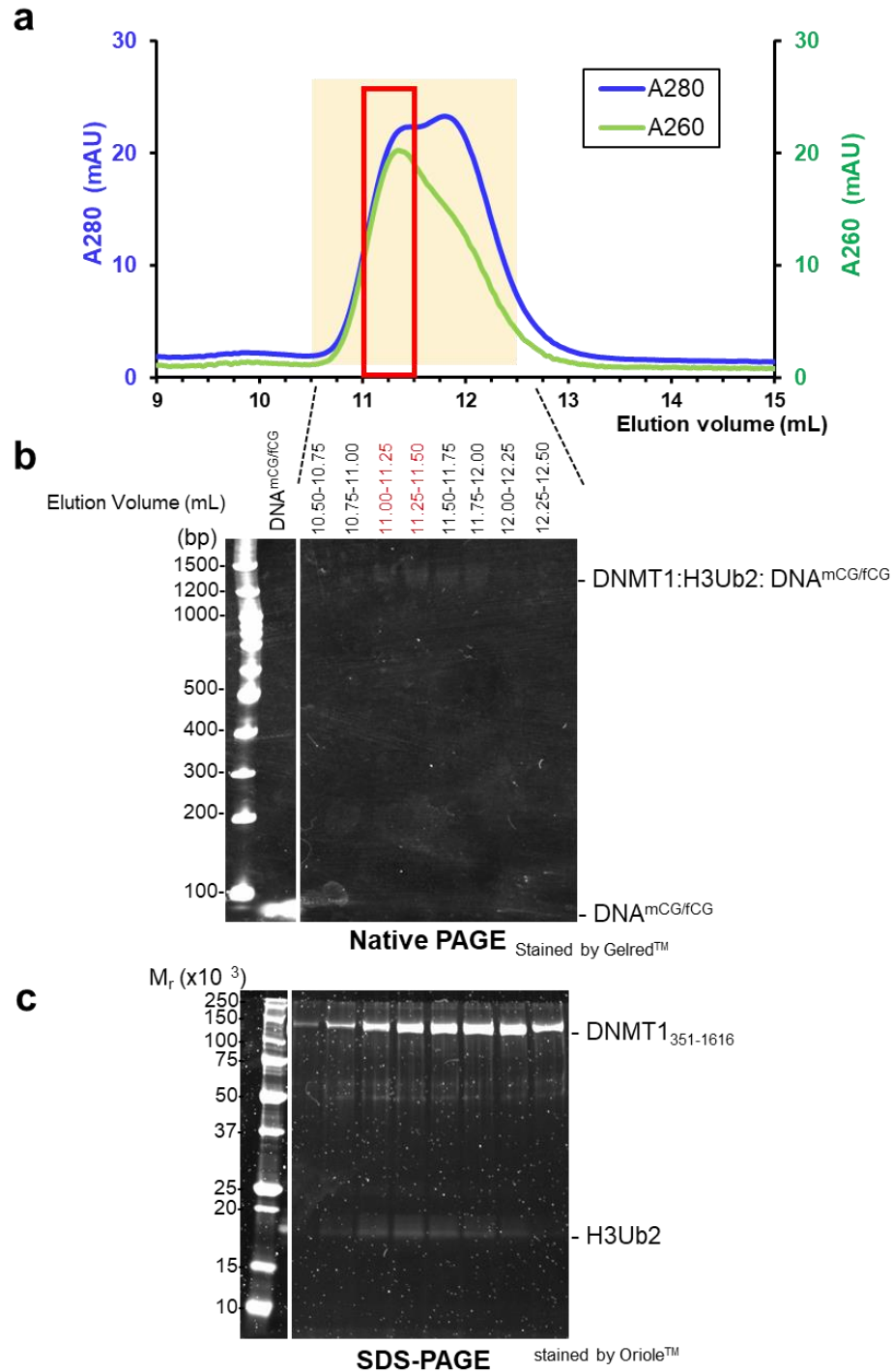
Extended Data Fig. 2 Sample preparation of DNMT1:H3Ub2:DNA$^{mCG/fCG}$ ternary complex for cryo-EM. **(a)** Size exclusion chromatography of the mixture of DNMT1:H3Ub2 binary complex and DNA$^{mCG/fCG}$. All fractions in the chromatography peaks were analyzed by **(b)** native-PAGE stained by Gelred^{TM} for detecting DNA and **(c)** SDS-PAGE stained by Oriole^{TM} for detecting proteins.
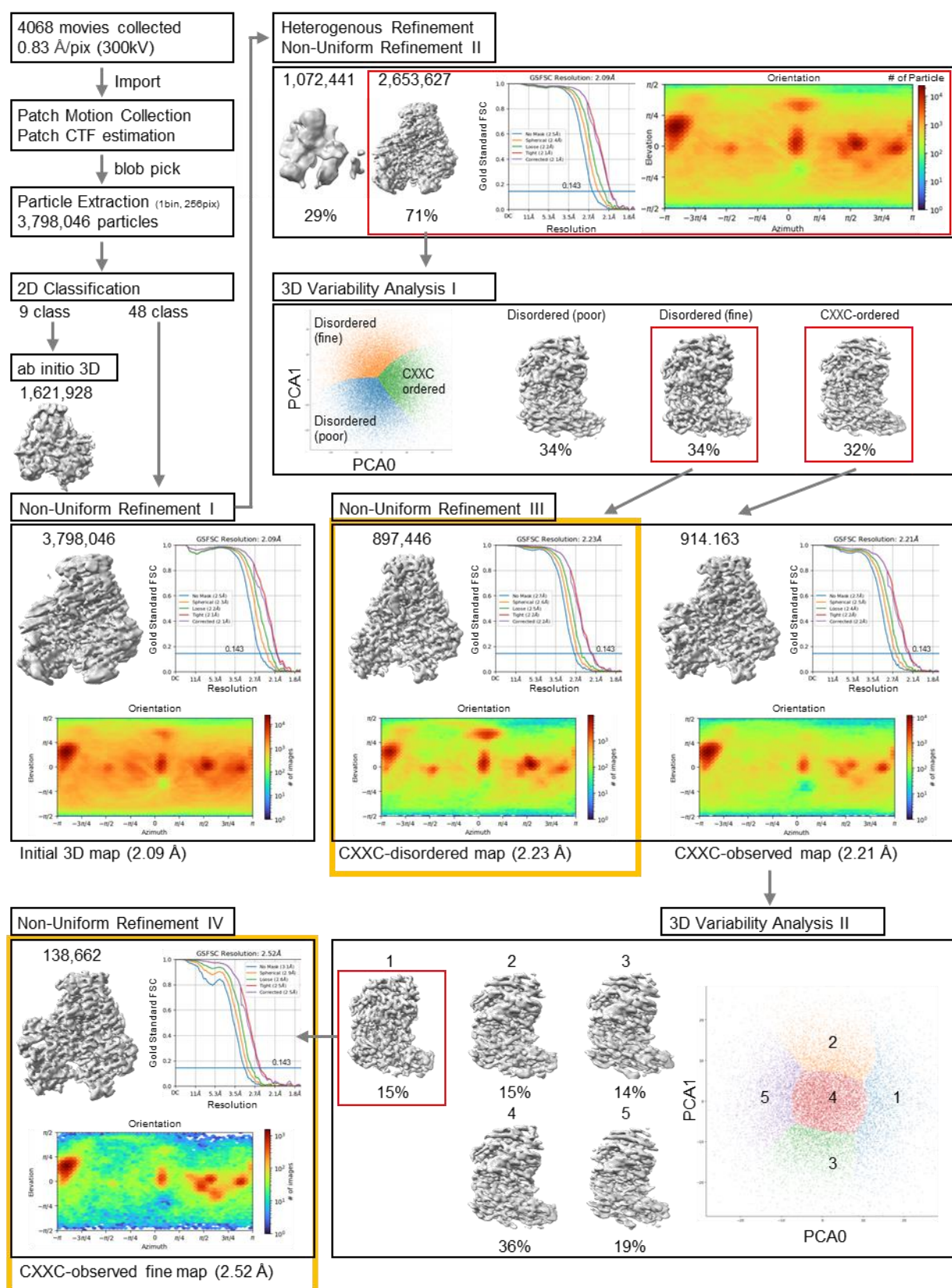
Extended Data Fig. 3 Overview of cryo-EM data processing workflow for DNMT1:H3Ub2:DNA[mCG/fCG]. Data processing were performed on cryoSPARC. 3,798,046 particles were automatically picked blob picker from 4,068

1   motion corrected movies. After the reference-free 2D classification, *ab initio* 3D model was constructed from the

2   best nine in the 2D classes. Then, Non-Uniform Refinement I was performed against all the extracted particles to

3   yield the cryo-EM map with an overall resolution of 2.09 Å resolution. The subsequent heterogeneous refinement

4   selected 2,653,627 particles as a good class. These particles were subjected to a 3D variability analysis, separating

5   the CXXC-ordered and CXXC-disordered models. The particles (138,662) in the CXXC-ordered model and those

6   (897,446) in the CXXC-disordered models were then subjected to Non-Uniform Refinement (III, IV) to generate a

7   cryo-EM map with an overall resolution of 2.52 Å and 2.23 Å, respectively.

8
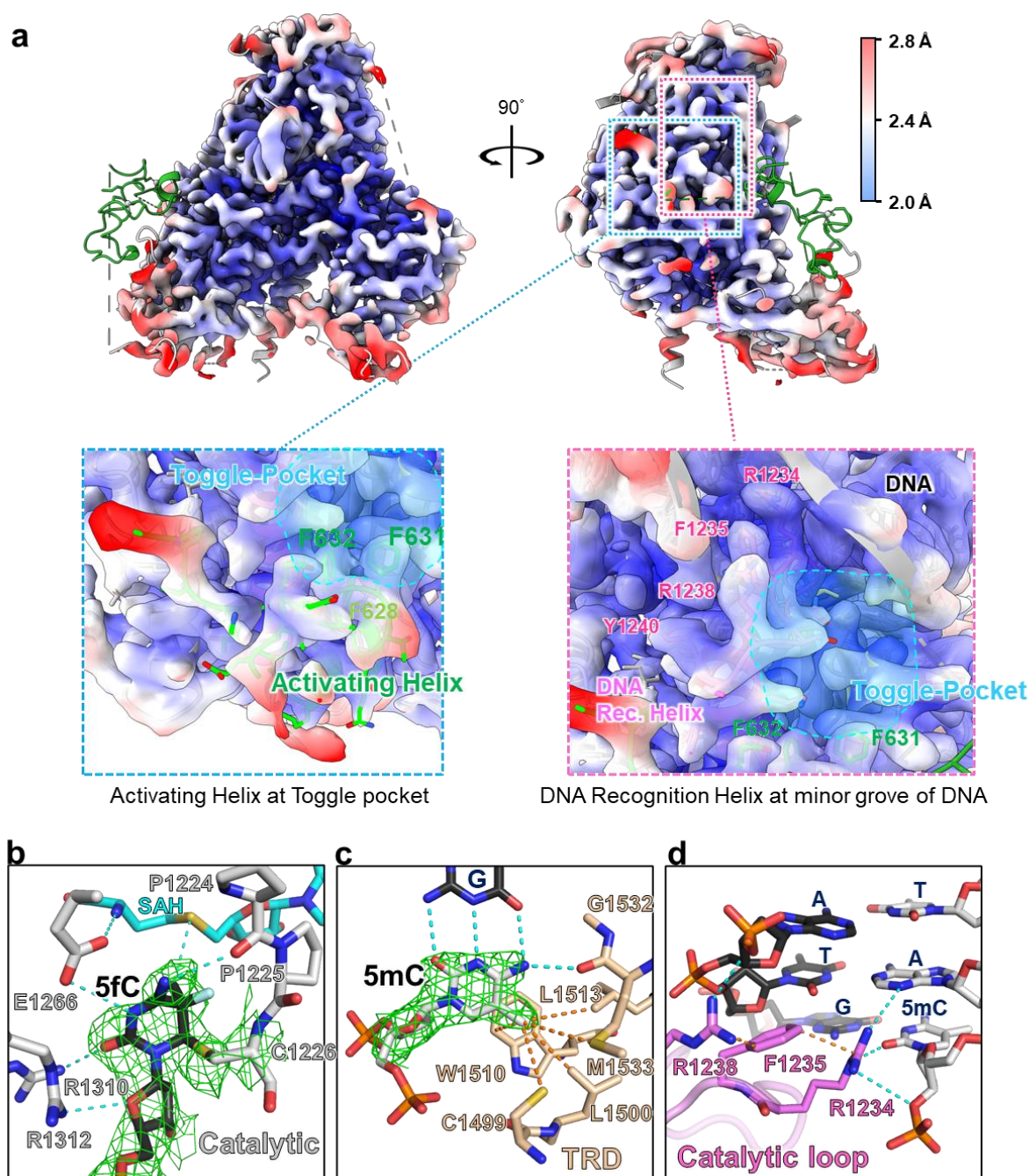
Extended Data Fig. 4 Local resolution map of CXXC-disordered DNMNT1:H3Ub2:DNA$^{\text{mCG/fCG}}$. (a) CXXC-disordered cryo-EM map of transparent surface were overlayed on the cartoon model of CXXC-ordered model by UCSF Chimera. CryoEM map from front view (upper left) and side view (upper right) were colored with the local resolution, which is estimated by cryoSPARC. Close-up view of the Toggle Pocket (lower left) and minor groove of DNA at mCG/fCG site (lower right) were depicted in lower panel. Stick model of CXXC-ordered model were shown in same color scheme with Fig. 1b. **(b)** Recognition of 5-fluolocytosine (5fC). 5fC, amino acid residues in the catalytic domain of DNMT1 and SAH are shown as black, gray and cyan stick models, respectively. Cyan dotted line indicates hydrogen bond. Green mesh shows cryo-EM map. **(c)** 5-methylcytosine (5mC) recognition by TRD

1   domain of DNMT1 showing light orange stick model. Cryo-EM map corresponding to 5mC was shown as green

2   mech. **(d)** Recognition of the DNA from the minor groove at 5mCG/5fCG site by catalytic loop of DNMT1. The

3   residues in the catalytic loop are shown as pink stick model.

4
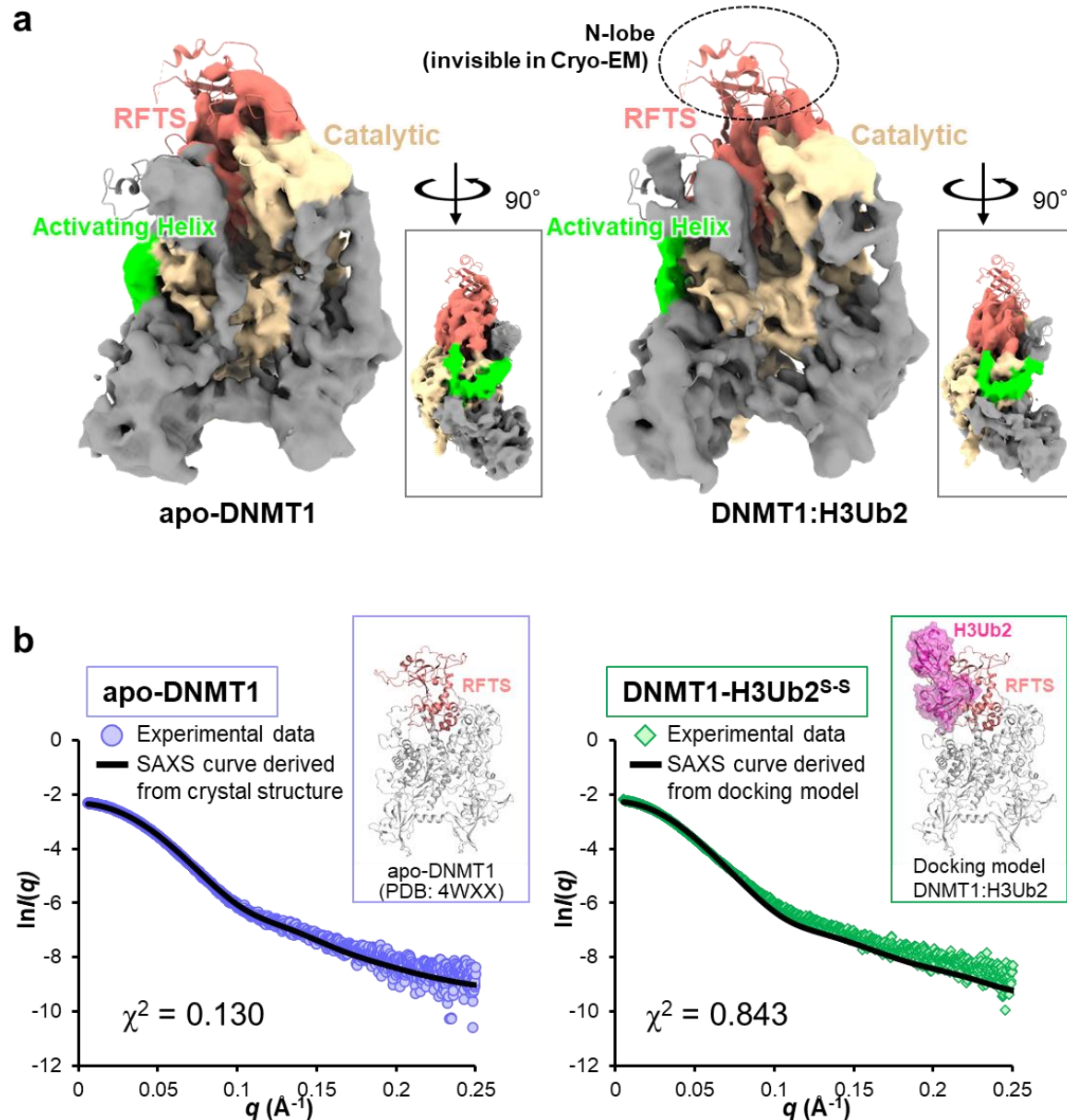
Extended Data Fig. 5 Structural analysis of apo-DNMT1 and it complex with H3Ub2. (a) Cryo-EM map of apo-DNMT1 (aa:351-1616, left) and the DNMT1:H3Ub2 binary complex (right). RFTS, Activating Helix and catalytic domains are colored salmon pink, green and beige, respectively. The cartoon model of crystal structure of apo-DNMT1 (PDB: 4WXX) is superimposed on the cryo-EM maps (EMD-33299, EMD-33298). **(b)** SAXS intensity data of apo-DNMT1 (purple circle) and DNMT1:H3Ub2^{S-S} complex (green triangle) superimposed on the theoretical scattering curves, showing black line, derived from crystal structure of apo-DNMT1 (PDB: 4WXX) and a model structure of apo-DNMT1 docking with RFTS:H3Ub2

1   complex (PDB:5WVO), respectively. The inset depicts the cartoon model of apo-DNMT1 and

2   the docking model of DNMT1:H3Ub2 complex.
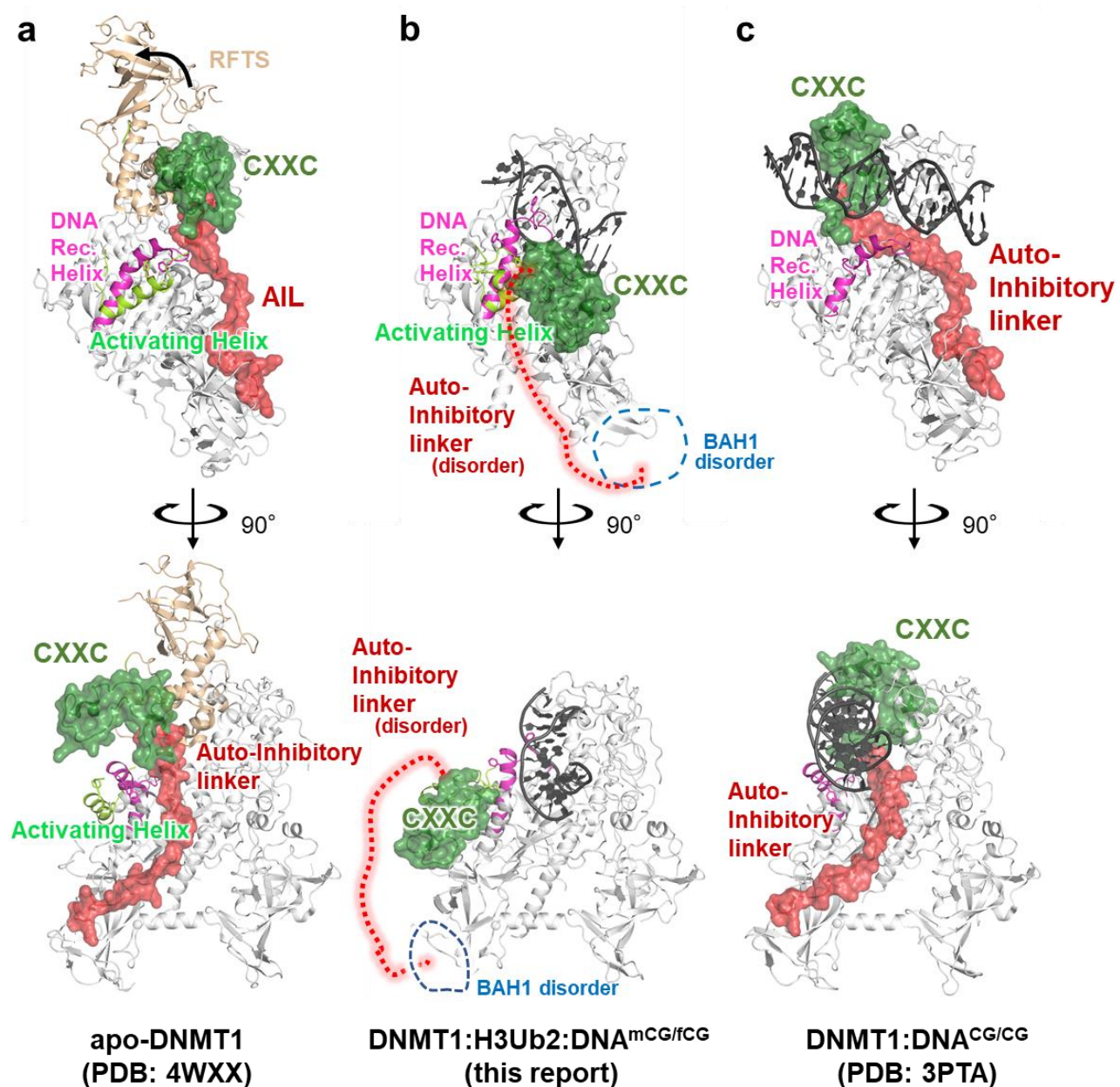
3
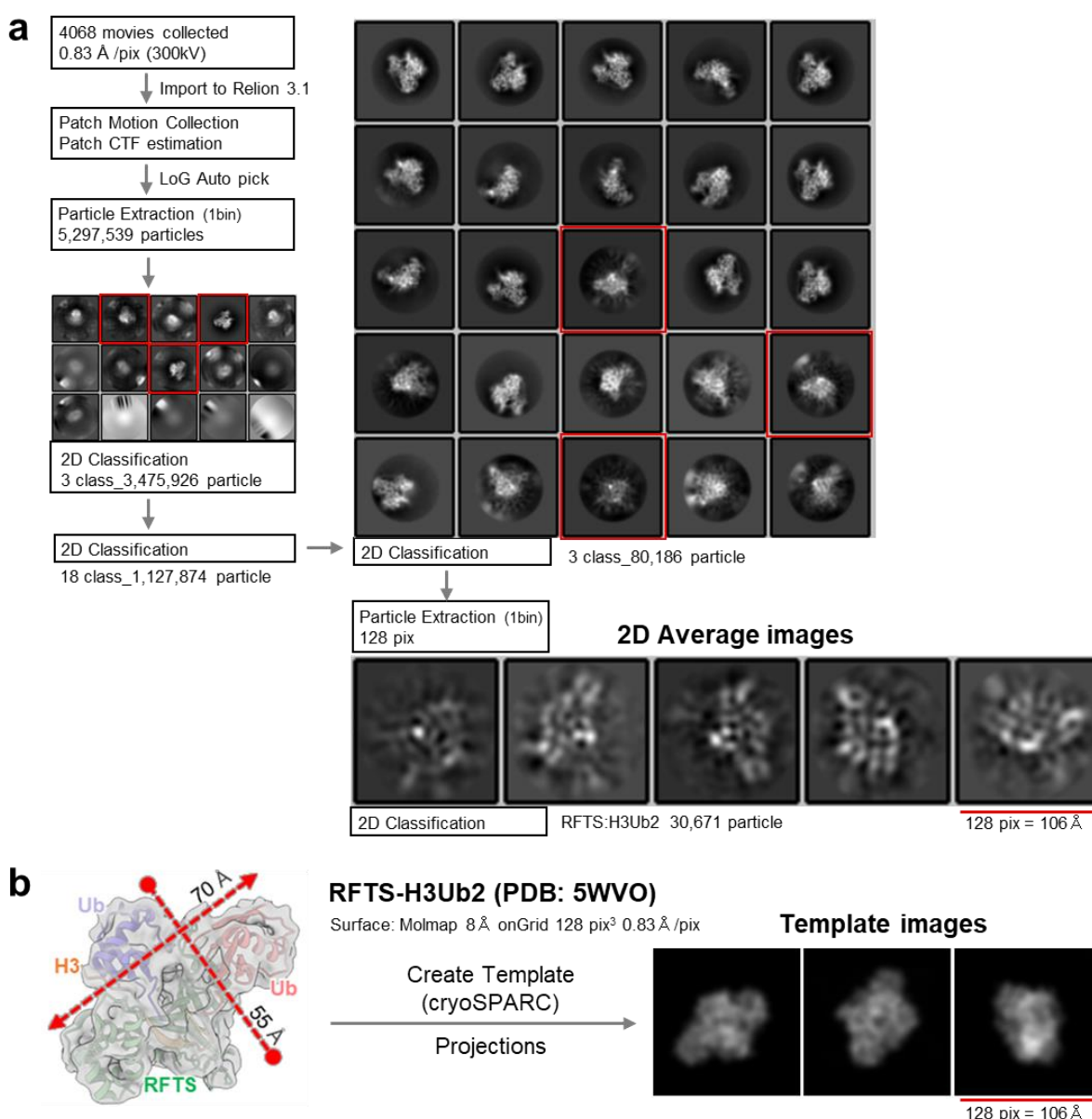
**Extended Data Fig. 6 Cryo-EM analysis of DNMT1:H3Ub2:DNA$^{mCG/fCG}$ using Relion 3.1.**

(a) Data processing were performed on Relion 3.1. Cryo-EM map refinement using Relion 3.1. 3,624,260 particles were automatically picked by crYOLO from 4,068 motion corrected movies. After the reference-free 2D classification, *ab initio* 3D model was constructed from the best nine in the 2D classes. The hand flipped *ab initio* 3D model of apo-DNMT1 (Supplemental Fig. 1) were used for the initial model. DNMT1 map was obtained after the single round of 2D classification and 2 rounds of Refine 3D. The final resolution was estimated as 2.3 Å by postprocess of Relion with soft mask. Single particle image was also extracted by LoG Auto picker of Relion to check the particles of other biomolecules. After three rounds of 2D

1   classification, the particle smaller than DNMT1 was selected. These smaller particles (80,186)

2   were re-extracted in a box size of 128 pixels with a 0.83 Å/pixel size, and the images were

3   classified by 2D classification. **(b)** The major 2D average images were compared with the

4   projected templates of H3Ub2-RFTS domain complex (PDB: 5WVO). Gaussian model of the

5   complex was created by the Molmap of ChimeraX. The 2D projected templates were created by

6   the module of "create template" in cryoSPARC.

7

8

9

10

apo-DNMT1
(PDB: 4WXX)

DNMT1:H3Ub2:DNA$^{mCG/fCG}$
(this report)

DNMT1:DNA$^{CG/CG}$
(PDB: 3PTA)

Extended Data Fig. 7 Domain rearrangement of human DNMT1 caused by H3Ub2 and hemimethylated DNA binding. Comparison of overall structure of **(a)** apo-DNMT1 (PDB:4WXX), **(b)** DNMT1:H3Ub2:DNA$^{mCG/fCG}$ ternary complex (this study), and **(c)** DNMT1:DNA$^{CG/CG}$ binary complex (PDB: 3PTA). Upper and lower panels show the side and front views of DNMT1, respectively. RFTS domain, Activating Helix, Auto-Inhibitory Linker, and DNA Recognition Helix were colored light orange, light green, red and pink, respectively. CXXC domain and Auto-Inhibitory Linker are also exhibited as the transparent surface model. The disordered regions of BAH1 and Auto-Inhibitory Linker are shown as dotted line.

1
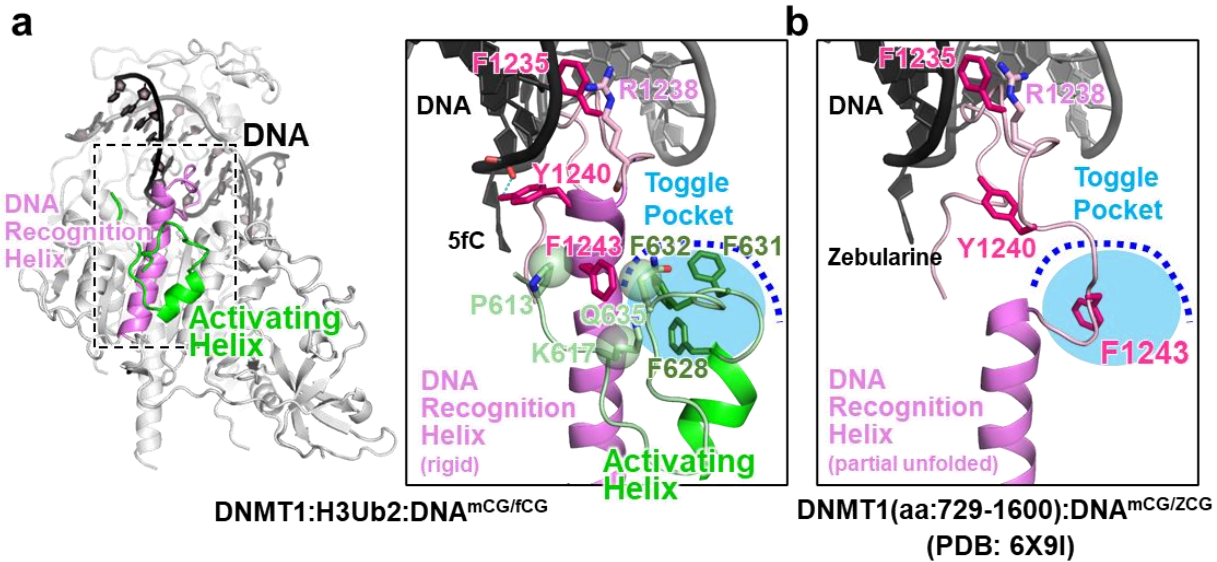
2 **Extended Data Fig. 8 Structural comparison of DNA recognition helix in the ternary complex and**

3 **DNMT1:DNAmCG/zCG binary complex (aa: 729-1600, PDB:6X9I). (a)** Structure of DNA Recognition Helix

4 (pink) and Activating Helix (green) of the ternary complex. Residues involving in recognition of DNA and

5 interaction with the Toggle Pocket are shown as stick model. Toggle Pocket is highlighted as light-blue. The cognate

6 DNA strands are colored as black and gray. **(b)** Structure of DNA Recognition Helix of DNMT1:DNAmCG/zCG

7 binary complex (z: Zebularine). Color schemes are same as (A).

8

1
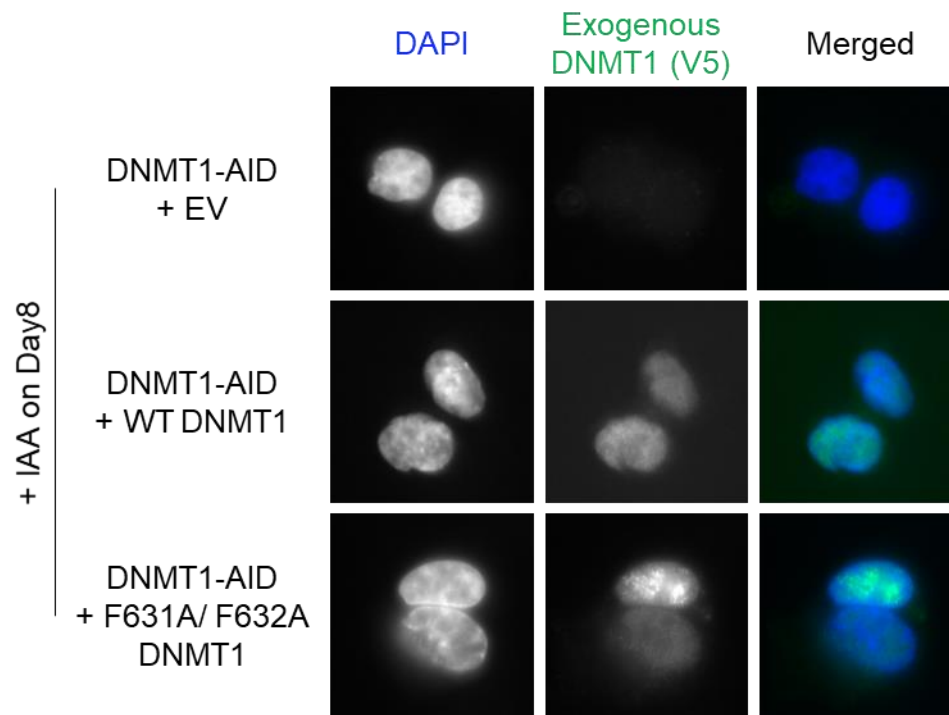
Extended Data Fig. 9 Nuclear localization of Exogenous DNMT1. The EV and exogenous V5 tagged DNMT1 (WT and F631A/F632A) were stably transfected to HCT116 cells expressing endogenous DNMT1-AID. The stable transfected cells were treated with IAA for 8 days. The nuclear was stained with DAPI, and exogenous DNMT1 was stained with V5 tag and second antibody. For merged images, the blue signal is corresponding to DAPI image, and the green signal is corresponding to exogenous DNMT1.